Distribution Agreement

In presenting this thesis as a partial fulfillment of the requirements for a degree from Emory University, I hereby grant to Emory University and its agents the non-exclusive license to archive, make accessible, and display my thesis in whole or in part in all forms of media, now or hereafter now, including display on the World Wide Web. I understand that I may select some access restrictions as part of the online submission of this thesis. I retain all ownership rights to the copyright of the thesis. I also retain the right to use in future works (such as articles or books) all or part of this thesis.

Shannon Catherine Hill April 9, 2018

The Mysterious White Dwarf G29-38: Can Magnetically Supported Outflows Explain the 10 μm Excess Emission in its Spectral Energy Distribution?

by

Shannon Catherine Hill

Dr. Alissa Bans
Adviser

Department of Physics

Dr. Alissa Bans

Adviser

Dr. Erin Bonning

Committee Member

Dr. Susanna Widicus Weaver

Committee Member

2018

The Mysterious White Dwarf G29-38: Can Magnetically Supported Outflows Explain the 10 μm Excess Emission in its Spectral Energy Distribution?

By

Shannon Catherine Hill

Dr. Alissa Bans

Adviser

An abstract of
a thesis submitted to the Faculty of Emory College of Arts and Sciences
of Emory University in partial fulfillment
of the requirements of the degree of
Bachelor of Sciences with Honors

Department of Physics

2018

Abstract

The Mysterious White Dwarf G29-38: Can Magnetically Supported Outflows Explain the 10 μm Excess Emission in its Spectral Energy Distribution?
By Shannon Catherine Hill

The spectral energy distribution of variable white dwarf G29-38 has an unusually strong near infrared emission feature as well as a strong 10-micron silicate feature. Previous models have attempted to explain G29-38's SED characteristics through various dusty disk and toroidal geometries, yet it is unclear how these models would be physically supported. As such, we investigate for the first time how the magnetic properties of G29-38 could result in magnetically supported outflows as modeled by disk winds and x-winds. We construct 72 different disk wind and x-wind models; highlighting models with novel geometries where the magnetic truncation radius is larger than the sublimation radius and the disk size scales with the Roche limit of corresponding planetary objects that we assume is the origin of the dust. We show how well the models reproduce the spectral features of G29-38 and also discuss their relevancy for the white dwarf system. We find that magnetically supported outflows do effectively simulate the spectral energy distribution features for the system, and that this proof of concept will motivate future work to further constrain the models for a more accurate picture.

The Mysterious White Dwarf G29-38: Can Magnetically Supported Outflows Explain the 10 μm Excess Emission in its Spectral Energy Distribution?

By

Shannon Catherine Hill

Dr. Alissa Bans

Adviser

A thesis submitted to the Faculty of Emory College of Arts and Sciences
of Emory University in partial fulfillment
of the requirements of the degree of
Bachelor of Sciences with Honors

Department of Physics

2018

Acknowledgements

I would like to first and foremost acknowledge my advisor Dr. Alissa Bans for her patience and undying optimism throughout this difficult process. Thank you for your excitement and consistent encouragement. Thank you for allowing me to explore a challenging research question and for valuing my contributions. This thesis was a large undertaking, but I heavily enjoyed our three-hour research meetings and I had a lot of fun working with you.

I would also like to extend my sincerest gratitude towards Dr. Erin Bonning for her constant support and understanding throughout the last three years of my undergraduate experience. Thank you for giving me the self-confidence to follow the curiosity of my mind, rather than the predetermined path prescribed by faceless institutions, and still find success You teach with an almost unparalleled sense of integrity and fairness. Your honesty and self-reflection has reminded me on many occasions that though the universe is endlessly fascinating, our lives on this planet hold potential much larger than that within our narrow academic interests. Thank you, Dr. Bonning. You have heavily influenced my direction and I would not be where I am without your generous time and energy.

I would also like to thank Dr. Pamela Scully. You have been integral to my growth as a human being. In the face of many obstacles, you've pushed me to embrace my academic impulses. Thank you for genuinely caring about my well-being and for saying "yes" when so many have said "no" to my aspirations. Thank you for always believing in me.

Of course, I would like to thank Donna Callihan-Hill, for her deep understanding of who I am. Thank you for reminding me that it's okay that I am young and that I don't know what I am doing. Thank you for reminding me that I am doing everything I can to learn and to take advantage of all the incredible opportunities around me. Thank you for showing me that taking risks, academic or otherwise, is a necessary precursor to accomplishing my dreams. Thank you, mom—your admission of my discomfort has been comforting.

Finally, thank you to my honors committee for your feedback and accommodations. I appreciate the time each of you spent in your evaluation of my work and I am thankful for your input and your advice for me moving forward.

Table of Contents

Table of Figures

Chapter I. Introduction

Inside of a star, the process of nuclear fusion transforms hydrogen into helium. During the late stages of stellar evolution, the helium produced inside the star starts to sink towards the center. The helium is then fused into the heavier elements of carbon and oxygen. Low to medium mass stars cannot reach a temperature high enough to further fuse carbon and oxygen into heavier elements. As a result, the carbon and oxygen collect in the center of the star as the star sheds its outer shell into a planetary nebula. The remaining carbon and oxygen stellar core becomes the extremely dense and hot white dwarf star. Without internal hydrogen or helium supplies, the structure of the white dwarf star is only supported by electron degeneracy pressure. The condensed mass of the white dwarf produces a large gravitational pull that creates a stratified stellar atmosphere of separate helium and hydrogen layers.

WD 2326+049, also known as Giclas 29-38 (G29-38), is the variable pulsating white dwarf star with the first DAZd classification. G29-38 was once an F or A star and has now been cooling as a white dwarf for 0.5 Gyr, which means it is a relatively young star (von Hippel et al., 2007). The variable luminosity of G29-38 is perplexing; it is the result of nonradial g-mode pulsations (Robinson et al., 1982). It is unclear which underlying mechanism is responsible for these pulsations, however the pulsation modes allow us to understand the inside environment of the white dwarf and the diffusion times of metals on the star's surface. The DAZd classification of G29-38 describes the star's dusty, metal rich characteristics. G29-38 has a pure hydrogen atmosphere and photospheric absorption lines from heavy elements like Ca, Mg, and Fe (Koester et al., 1997). The amount of time it takes for Ca to diffuse from the surface of the star is less than the evolutionary time scale for G29-38 (Koester, 2009). Therefore, the presence of Ca on the surface indicates that the white dwarf must be accreting these metals from an external source.

Suggestions for the external source of metals have ranged from the interstellar medium (ISM) (Dupuis et al., 1992, 1993a, b), the discrete accretion of comets (Alcock et al., 1986), and a tidally destroyed asteroid (Jura, 2003).

G29-38 is also the first white dwarf found to have extremely bright (~3% of its bolometric luminosity) near infrared (NIR) excess (Zuckerman & Becklin, 1987; Reach et al., 2005). Initially, it was thought that the infrared excess of G29-38 was also connected to the ISM or due to a Jupiter-sized or brown dwarf companion. However, subsequent observations through speckle imaging (Kuchner et al., 1998) did not reveal any such companion. Any planets that could be in the G29-38 system are currently undetected (Debes et al., 2005). Dust reradiates strongly in the infrared, therefore some large surface area or some stream of dust could be producing the signal. The stream of dust could be from the ISM or it could be from some sort of structure that was broken up by the gravity of the white dwarf. ISOCAM observations did not support ISM accretion (Chary et al., 1998). This leaves the possibility that the NIR excess could be the result of some distribution of particles from a tidally destroyed object.

In further support of some particulate responsible for the external source of accreted metals and the NIR excess emission, observations of G28-39 with the *Spitzer Space Telescope* revealed a 10-micron feature in the spectral energy distribution of the star. The 10-micron feature is likely due to silicate particles which reradiate strongly at those wavelengths (Reach et al., 2005) The silicate particles need to be at the semi cool temperatures of 290-890 K for such a strong 10-micron emission, which places the grains far from the star. Though for G29-38, the luminosity of 2×10^{-3} $L_{\odot}$ may place the grains only a few stellar radii away (Jura, 2003; Reach et al, 2005a).

Many orientations of dust geometry have been modeled to explain the spectral energy distribution of G29-38 such as a flat, opaque thin disk (e.g. Jura 2003; Reach et al., 2005; Reach

et al., 2009;) or an extended torus (Jura et al., 2007; Jura et al., 2008). Many models can describe the observed spectral energy distribution reasonably well, some of which require 10^{24} g of dust (Jura, 2003) while others require just 10^{19} g (Reach et al., 2009). Therefore, modeling the spectral energy distribution boils down to a problem of finding a dust distribution that can catch enough stellar light and determining how much dust is necessary to recreate each spectral energy distribution emission feature.

The silicate feature in the spectral energy distribution may be explained by some type of dusty disk surrounding G29-38, but the photospheric absorption lines from multiple heavy elements imply an accretion process is also occurring. The mechanism that connects the accretion and the observed NIR excess is not well understood. However, the greater likelihood of an accreted Ca polar distribution compared to an accreted Ca equatorial distribution offers the first evidence that the accretion process onto G29-38 is affected by a magnetic field (Thompson et al., 2010).

When stars are compressed, their magnetic fields are strengthened due to the conservation of magnetic flux. However, this process involves large mass loss and is not well understood. Until recently, the magnetic properties of G29-38 were unknown. G29-38 shares a similar pulsation-frequency to HR 3831, a roAp star (Kurz & Martinez, 2012), and roAp stars have a cyclic frequency variability that suggest the presence of an internal mechanism of a magnetic cycle (Duerbeck, 2005). Around 10% of white dwarfs have global magnetic fields with magnitudes of 1kG to 100s of mG (Fusillo et al., 2017). However, Zeeman splitting is undetectable for magnetic fields less than or equal to 20kG (Jordan et al., 2007), leaving spectrapolarimetry as the only current option to identify magnetic white dwarfs (Fusillo et al., 2017). Circular spectrapolarimetry determined the upper limit magnetic field strength for G29-38 to be 2.5 kG, yet under the magnetic field limits from the high-resolution optical spectra of G29-38, the upper limit is instead estimated

at 20 kG (Farihi, 2017). Magnetic fields of 0.1 - 1 kG are of a sufficient magnitude to significantly affect dust dynamics and to impact the silicate particles surrounding G29-38 (Farihi et al., 2017). Fields at this strength can truncate a disk at the Alfven radius and result in accretion onto magnetic polar regions (Farihi et al., 2017). Therefore, the lower limit of 2.5 kG is enough to match the polar accretion of G29-38. The magnetic field range of 2.5 kG to 20 kG is consistent with our picture of magnetospheric accretion.

The magnetic properties of G29-38 complicate the dust-star interaction. It is clear from observations that dust is a necessary foundation to explain the spectral energy distribution, and it is clear that the stellar magnetic field plays a role. The disk models previously described do not take these magnetic properties into account. The flared torus disk model also lacks physical foundation. There is observational evidence that connects accretion disks around protostars, massive stars, and brown dwarfs with magnetic outflows (Pudritz et al., 2006). Thus, a better, physically motivated model to explain a vertically supported dust structure and the underlying accretionary picture is magnetic outflows. However, outflows and accretion in white dwarf systems have been observed only in close binary systems or cataclysmic variable systems (e.g. Hermes et al., 2013; Froning et al., 2004; Sokoloski & Kenyon, 2003). Therefore, outflows and accretion have only been studied in white dwarf two-star systems. In this study, we explore whether a magnetically supported vertically distributed outflow, modeled by disk winds or x-winds, could accurately produce the NIR emission and the silicate emission features in the isolated white dwarf G29-38's spectral energy distribution.

Chapter II. The Development of G29-38 Outflow Models

The characteristics of the spectral energy distribution, the evidence of magnetospheric accretion, and the newly quantified magnetic parameters of G29-38 imply that outflows may be relevant to the overall picture of the star-disk system. Disk winds and x-winds are potential examples of magnetically supported outflows. As white dwarf accretion and outflows have only been studied in binary systems, we examined the G29-38 system by developing our own physically supported outflow models by adapting disk winds and x-winds to the isolated system.

Wind Types

Disk Winds

Disk winds are centrifugally driven outflows that result from magnetic field lines threading a circumstellar disk. The circumstellar disk is made up of neutral gas, ions, and dust. When the magnetic field lines thread the disk, they pass a magnetic torque to the disk material. The magnetic torque translates into angular momentum and the material travels towards the center of the disk. The radial motion of the disk material bends the magnetic field lines away from the disk's axis of rotation (Blandford & Payne, 1982). Ions within the disk travel along the magnetic field lines and collide with the neutral material within the disk. These collisions cause the neutral matter to lift up dust grains. Due to the rotation of the disk and the bent magnetic field lines, large amounts of dust grains and neutral material can be flung out from the disk, culminating in a centrifugally driven outflow (Safier, 1993b).

In the protostellar case, circumstellar disks are formed from the collapse of magnetically supported molecular cloud cores, which subsequently thread the disk with open field lines (Königl & Pudritz, 1999). In Bans et al. (2012) simulated dusty outflows have been successful in recreating large amounts of near IR excess seen in luminous protostars as well as a strong 10-micron feature.

Therefore, we retrofitted a code that was built to handle the geometries of disk winds in the protostellar system to the white dwarf system (*See Chapter III*).

To model a dusty disk wind, we needed the gas-dust ratio of the wind as well as the gas density profile. We used a constant gas-dust ratio of 100, because while the actual ratio of gas to dust may change, good fits to the protostellar spectral energy distribution have been found with this ratio (Bans et al., 2012). Semi-analytical gas density structures have been calculated for disk winds (Safier, 1993b). We chose the three representative wind solutions used in Bans et al. (2012). Each wind solution is characterized by a particular magnetic field line shape and density distribution. Wind model C produces the most vertical magnetic field lines (*See Figure 1*). This is an important feature regardless of the wind density because it gives wind model C the potential to intercept the most starlight. This is particularly relevant when analyzing the flux levels and the inclination effects of our results (*See Chapter IV)*.

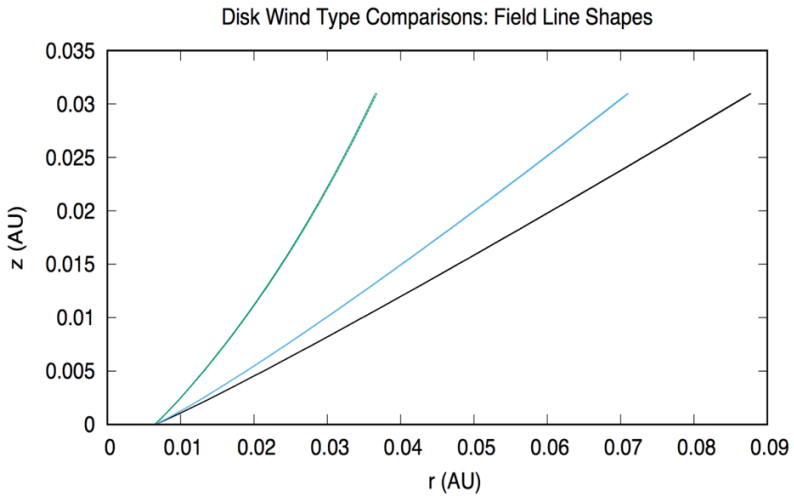

Figure 1. The magnetic field lines are shown by comparing the first streamline at the truncation radius with length of field line along the x-axis and height of field line along the y-axis. Wind model C (green) has the most vertical of field lines, then wind model G (blue), and then wind model E (black).

Wind model C also decreases the least in density as it extends upwards with height (*See Figure 2*). This is important for our white dwarf system because the SED of G29-38 has two features, a hotter NIR excess feature and a cooler 10-micron feature. To recreate those characteristics, we require a geometry that can capture starlight closer to the star where it is hotter, and we require a geometry that can capture starlight further from the star where it is cooler (*See Figure 3*). The cooler 10-micron feature can result from wind that is closer to the disk but further from the star in radial distance, or from wind that is closer to the star in radial distance but at a far enough vertical distance (the top of the wind) that it is still at a cooler temperature. However, if

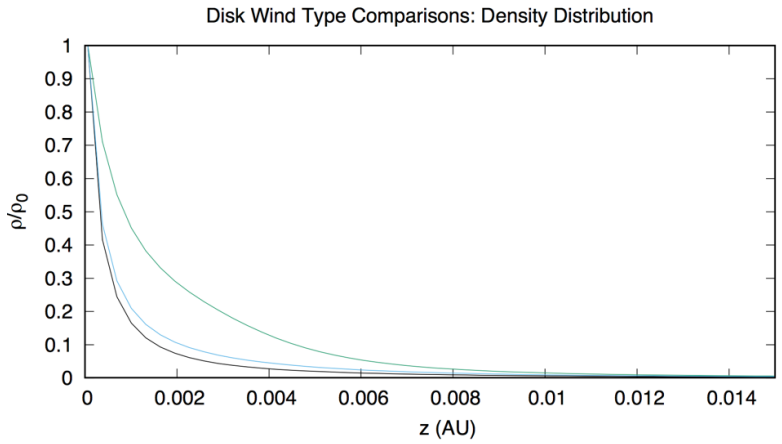

Figure 2. The normalized density of wind model C (shown in green), wind model E (shown in blue), and wind model G (shown in black)

the wind drops too much in density as it is increasing in height it could become transparent and not absorb stellar emission. Thus, wind model C has an advantage due to it flatter density profile with height; the greater density the wind has as it extends further from the star, the more likely we will be able to recreate both the NIR excess feature and the silicate feature of the spectral energy

distribution. Therefore, while each disk wind model is relevant to the system at hand, we chose to model our simulated disk winds under the parameters of disk wind model type C.

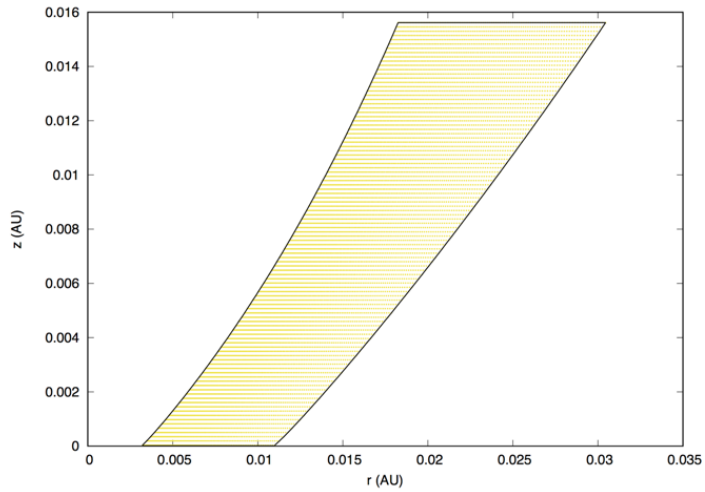

Figure 3. The shape of the full model C disk wind. The x-axis can act visually as the extent of the accretion disk in AU as the y-axis shows the outflow's vertical component. Here the wind was launched from our minimum truncation radius described in Table 1.

X-winds

Unlike disk winds, x-winds are the result of direct star-disk interaction. Stellar magnetic field lines can interact with the accretion disk directly by acting like open field lines and threading the disk in a similar process to that involving disk winds (Königl & Pudritz, 1999). However, the stellar magnetic field truncates the disk at a narrow "x-region", rather than spreading across several radii like the disk wind magnetic field. A centrifugally driven outflow that is launched from the x region is called an x-wind. The x-wind is much narrower and more compact than the disk wind. As the x-wind is ultimately driven from stellar field lines, there is also a "funnel flow" occurring towards the star. This funnel flow is responsible for polar accretion, a characteristic of the G29-38 star-disk system. For a detailed schematic of an x-wind model system, see *Figure 1* in Shu et al. (1997).

Just like the disk wind, to model the x-wind we require a dust distribution within the wind and a gas density structure. We used the same gas-to-dust distribution ratio of 100 as in the disk winds. Unlike the disk winds, there are no semi-analytical solutions for x-wind gas density structures. However, the code we used just requires the description of the outflow shape, whether that be a disk wind or an x-wind. Therefore, we used the magnetic field line profile and vertical density profile of a typical x-wind from Shu et al. (1997) to construct a toy model for the x-winds simulated in this project. We did our own analytical fits of the density profiles and streamline shapes from the x-wind described in *Figure 2* from Shu et al. (1997) and then scaled these fits to the G29-38 system (*See Figure 4*).

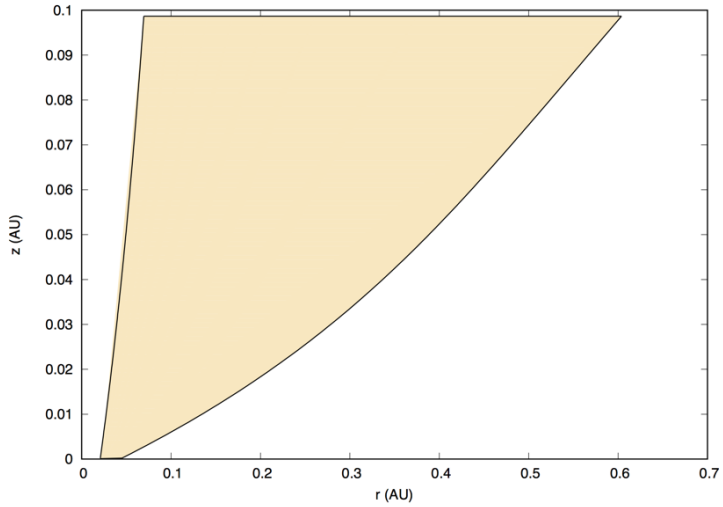

Figure 4. The shape of the full x-wind. The x-axis shows the width of the wind, which at the base of the wind is approximately 10% of the launching radius. The y-axis shows the outflow's vertical component. Here the wind was launched from our maximum truncation radius described in Table 1.

To recover the location of the streamlines at distances far from the x-wind origin, an initial wind density is required. We scaled the initial wind density with the mass of the disk and the mass of the wind determined by our models. X-winds almost all launch at the same density as it is a narrowly launched outflow when compared to disk winds. The x-wind is quite vertical, and the

density is not as stratified as the disk wind (*See Figure 11*). One limitation we faced in constructing these analytical fits and building our own x-wind toy model is the x-wind narrow launching zone. Our code needs to divide the wind into zones as well as requires a unique radial location for every "footprint" of the streamline. It is very difficult for the code to resolve different regions of streamlines that spread out at large heights but are extremely close together when close to the disk. Thus, we were forced to increase the x-wind launching point near the disk surface. The radial width of the launching region was about 10% of our launching point.

The underlying mechanisms of outflows is still contested. Most outflow models of magnetically driven winds use centrifugal forces as the main launching mechanism to eject material along inclined field lines (Edwards et al., 2006). Though we have some ideas about which outflow type would be more relevant to G29-38 (*see Chapter V*), the main difference between our models is that the x-wind model has a narrower launching region and a much denser distribution as the wind height increases. It is possible that some of our disk-wind models, if launched in a narrow region comparable to the x-wind launching region, could be good approximations for x-winds with different efficiencies. This is still to be studied as we did not use true analytical solutions for an x-wind.

Model Parameters

This project simulated 72 different models for the spectral energy distribution of G29-38 (*See Table A.1 in Appendix A for full details of each model*). We constructed 36 different theoretical models for the disk winds and 36 different theoretical models for the x-winds.

Inner Boundary of Disk

Usually the innermost location that dust in the disk or the wind can be found at is the sublimation radius. The sublimation radius R_{sub} is the point at which the temperature of the interstellar dust grains reaches the grain sublimation temperature typically from heating due to stellar radiation. As the sublimation radius depends on the stellar flux, it is usually scaled as

$$r_{sub} \propto {L_*}^{1/2} \quad [2.1]$$

due to the inverse square dependence of the radiative flux on distance from the source. Using 2 x 10^{-3} $L_\odot$ for the luminosity of G29-38, we calculated the sublimation radius for 1-micron pure silicate grains with optical properties from Weingartner & Draine (2006) to be 0.0025-0.0035 AU (or 3.74 x 10^{10} – 5.24 x 10^{10} cm) assuming a sublimation temperature of 1250-1500 K. Aside from the luminosity dependence mentioned above, sublimation radii depend on grain properties such as composition and size. Therefore, smaller sublimation radii estimations for G29-38 have been reported to be 0.001-0.002 AU (or 1.65 x 10^{10} cm – 2.54 x 10^{10} cm) that take into account inner disk heating effects and grains of different types (von Hippel et al., 2007).

However, the inner radius of the circumstellar disk would also be affected by the magnetic field of G29-38. Previous disk models for G29-38 have not accounted for this effect. As any circumstellar disk gets closer to a magnetic star, it experiences a stronger magnetic field. At some point, the magnetic field disrupts the Keplerian flow of the disk as the field lines thread the disk and transport angular momentum to the star. This means that the inner edge of the disk is located where the rate that the stellar magnetic field removes angular momentum from the disk is greater than the internal viscous stress (Wang, 1996). This inner edge is referred to as the magnetic truncation radius r_M.

The magnetic truncation radius is difficult to calculate directly due to its dependence on magnetic torque. In the star-disk interaction, the magnetic torque on the disk depends on how well

the magnetic field lines thread the disk (Ryden, 2011; Wang, 1996). However, the Alfven radius r_A for spherical accretion is related to the magnetic truncation radius by some coefficient that takes into account the angular momentum transfer in disk accretion not seen in spherical accretion:

$$r_M = \xi r_A. \quad [2.2]$$

Different simulations of stellar magnetic field-disk interactions have analytically determined the coefficient value to be 0.5 or 1, depending on how well the magnetic field penetrates the disk (Long et al., 2005; Wang, 1995).

The Alfven radius r_A is equal to the distance away from the star where the magnetic energy density of the stellar magnetosphere equals the kinetic energy density of the material in the surrounding disk (Ryden, 2011):

$$\frac{B^2}{(8\pi)} = \frac{\rho v^2}{2}. \quad [2.2]$$

Assuming a dipolar magnetic field and that the matter in the disk is in orbital free fall,

$$B = \frac{\mu}{{R_*}^3}\ ,\ v = \sqrt{\frac{GM_*}{r_A}}, \quad [2.3]$$

and using the equation of mass continuity,

$$\dot{M} = 4\pi {r_A}^2 \rho v \quad [2.4]$$

the Alfven radius r_A is

$$r_A \approx \sqrt[7]{\frac{\mu^4}{\dot{M}^2 G M_*}}\ . \quad [2.5]$$

In equation [2.5] μ is the magnetic moment calculated by equation [2.3], G is the gravitational constant, M_* is the mass of the white dwarf, and $\dot{M}$ is the accretion rate of the white dwarf. Due to the lack of clarity surrounding the direct calculation of r_M and surrounding the relationship between r_A and r_M, we decided to calculate r_M for G29-38 using the Alfven radius and a coefficient of 0.5 and 1. Using the previously described upper and lower limits for the magnetic

field, as well as an estimated accretion rate of 6.5 x 10^8 g/s for G29-38 (Xu et al., 2014), we calculated a range of potential truncation radii to use in our models. The calculated magnetic truncation radii are shown in *Table 1*.

Magnetic Field Limits	**Alfven radius relationship**	**Magnetic Truncation Radius**
2.5 kG	$R_M = 0.5R_A$	4.7053 x 10^{10} cm
	$R_M = R_A$	9.4106 x 10^{10} cm
20 kG	$R_M = 0.5R_A$	1.5440 x 10^{11} cm
	$R_M = R_A$	3.0879 x 10^{11} cm

Table 1. The Calculated Values for the Magnetic Truncation Radius of G29-38

For all values of the magnetic truncation radius that we calculated, $R_{sub} < R_M$. This is very much unheard of in the protostellar case. The magnetic truncation radius is usually closer to the star than the sublimation radius. Typical protostellar scaling places the magnetic truncation radius at about 3 times the radius of the star, with the sublimation radius approximately 50 times further out. A magnetic truncation radius with this scaling for G29-38 and our calculated sublimation radii for G29-38 would place a modeled outflow at temperatures much higher than the 290-890 K estimated for the spectral features and we would subsequently overproduce the NIR emission. This implied to us that in our models, the wind must start further from the star.

While dust would normally exist just past the sublimation radius, we find that this location is interior to the truncation radius even for our models with lower magnetic field strengths. Therefore, in all of our constructed models, we use a novel geometry with dusty outflows starting at the magnetic truncation radius (i.e. the inner edge of the disk) rather than the nominal sublimation radius. The inner disk radius at values equivalent to the magnetic truncation radius places the disk further away from the star than previously explained with the protostellar scaling. Subsequently, the outflows will be much cooler and could provide an opportunity for a better NIR excess fit.

To further assess the feasibility of this model geometry, we calculated the corotation radius, which is where the Keplerian frequency of the disk is the same as the rotational frequency of the star.

$$r_C = \sqrt[3]{\frac{GM_*}{\omega^2}} \quad [2.6]$$

The relationship between the corotation radius and the magnetic truncation radius directly affects the outflow accretion process. Asteroseismological techniques estimate the rotation rate of G29-38 at 0.55 km/s (Kawaler, 2003). Therefore, we calculated the corotation radius to be 2.92 x 10^{11} cm, which is very close to the magnetic truncation radius of 3.0879 x 10^{11} cm. If $r_M > r_C$, accretion is at a low rate and fits well with a steady-state accretion picture. If $r_C > r_M$, accretion is episodic (Spruit & Taam, 1992). The observed Ca II K-line Equivalent Width (EW) strength variability of G29-38 indicates that the accretion of G29-38 does not match the theoretically supported steady-state model and is instead episodic (von Hippel & Thompson, 2007). Our calculated r_C is greater than most of the r_M that we use, hence our models are consistent with these physical considerations.

Scaling the Outer Boundary and Mass of the Models

In Jura (2003), the flat disk model fitted to the spectral energy distribution happened to be comparable to the Roche limit of one asteroid. This project expands on the idea of Roche limit scaling by purposefully scaling the outer disk radius to the Roche limits of multiple objects with different masses (*See Table 2*). We explored three different types of objects that could have been tidally destroyed to create the disk plus outflow system: asteroids, terrestrial Earth massed planets, and gaseous Jupiter-massed planets. The progenitor of the accretion disk could be any of the

objects described, and this type of scaling is a nice way to explore the mass needed for the SED as well as its origins.

Object	**Roche Limit R_L *cm***	**Disk Radius (R_L x 5) *cm***	**(R_L x 10) *cm***	**(R_L x 11) *cm***
1 Asteroid	7.6667 x 10^{10}	3.8334 x 10^{11}	--	--
3 Asteroids	7.6667 x 10^{10}	3.8334 x 10^{11}	--	--
5 Asteroids	7.6667 x 10^{10}	3.8334 x 10^{11}	--	--
1 Earth	5.2779 x 10^{10}	2.6389 x 10^{11}	5.2779 x 10^{11}	--
3 Earths	3.6595 x 10^{10}	1.8298 x 10^{11}	3.6595 x 10^{11}	--
5 Earths	3.0866 x 10^{10}	1.5433 x 10^{11}	3.0866 x 10^{11}	4.6299 x 10^{11}
1 Jupiter	8.6648 x 10^{10}	4.3324 x 10^{11}	--	--
3 Jupiters	6.0080 x 10^{10}	3.0039 x 10^{11}	6.0080 x 10^{11}	--
5 Jupiters	5.0673 x 10^{10}	2.5336 x 10^{11}	5.0673 x 10^{11}	--

Table 2. Each object has a corresponding Roche limit R_L. For the asteroid objects, the assumption was made that multiple asteroids could have entered the system at once, therefore an increase in the number of asteroids does not lead to an increase in the corresponding Roche limit.

For constant density, setting the estimated tidal pull from the primary object equal to the self-gravity of the smaller object gives the following formula for the Roche limit:

$$R_{roche} = R_p \sqrt[3]{\frac{2M_*}{M_p}} \qquad [2.7]$$

where M_* is the mass of the star, M_p is the mass of the smaller object, and R_p is the radius of the smaller object. There are limitations with this Roche radius equation as it assumes a constant density scaling with mass. This is not exactly accurate in the gas giant case. However, the effects of a constant density assumption would not affect the Roche limit in such a way for gas giants that the overall results of the system would be compromised.

We set the outer radius of the disk to scale with the Roche limit for the objects of different masses mentioned above. We typically used an outer boundary of 5 times the Roche limit, though in the cases where the magnetic truncation was larger than this scaling, we extended the disk to 10-11 times the Roche limit. Typically, asteroids come in a range of masses. We chose the representative asteroid mass to be that of 10 Hygeia, a C-type asteroid. 10 Hygeia is the most

physically appropriate asteroid because of its physical characteristics. Reach et al. (2009) presents a disk model for G29-38 that requires the presence of water-ice to fit the spectral energy distribution. There are also theoretical calculations that show extrasolar planetesimals with internal water can survive the expansion in red giant stage of their parent star (Xu & Jura, 2014). Similarly, different types of meteorites have been analyzed with the polluted atmosphere of G29-38 to better understand the parent body that accreted onto the star. Bulk Earth, CR chondrites, primitive chondrites, and mesodiderites have been found to 95% confidence (Xu & Jura, 2014). 10 Hygeia's surface contains primitive carbonaceous matter similar to that of carbonaceous chondrite meteorites as well as aqueous products that could indicate a past presence of ice-water (Barucci et al., 2002). Therefore, it is a physically motivated model parameter. 10 Hygeia's mass is 8.276 x 10^{22} grams (Pitjeva & Pitjev, 2016).

The mass of the wind directly depends on the mass of the disk, but the exact relationship is unknown. However, the mass of the disk is what feeds the mass of the wind, therefore the disk should be more massive. For consistency, we scaled the mass of the wind to one-hundredth of the mass in the disk, where the masses of the total system (disk and wind) were equal to our representative masses of objects that could have been tidally broken up (*See Table 3*).

Object	**Disk Mass (grams)**	**Wind Mass (grams)**
1 Asteroid	8.276 x 10^{22}	8.276 x 10^{20}
3 Asteroids	2.483 x 10^{23}	2.483 x 10^{21}
5 Asteroids	4.138 x 10^{23}	4.138 x 10^{21}
1 Earth	5.972 x 10^{27}	5.972 x 10^{25}
3 Earths	1.792 x 10^{28}	1.792 x 10^{26}
5 Earths	2.986 x 10^{28}	2.986 x 10^{26}
1 Jupiter	1.898 x 10^{30}	1.898 x 10^{28}
3 Jupiters	5.694 x 10^{30}	5.694 x 10^{28}
5 Jupiters	9.400 x 10^{30}	9.400 x 10^{28}

Table 3. Shown above is the mass of the disk corresponding to the object for which the disk radius is scaled as well as the matching mass of the wind for each object.

In our models, the mass of the wind includes the mass of the dust as well as the mass of the gas. With the scaling parameter of the wind mass to one-hundredth of the disk mass, we checked each of our models to make sure that the upward pressure on the wind was much greater than both the stellar gravity and the disk gravity acting on the wind.

Wind Thickness and Disk Thickness

In each model, a physically thin disk was used, scaled to a height of $\sim .001 R_{sub}$. We used a thin disk to avoid a larger inner rim that would potentially obstruct the photons from reaching the outflow. An inner rim would affect our results because the main thing we are exploring is the effect of the dusty outflow itself. Bans et. al (2012) suggests that in the protostellar case the wind could be self-limiting. This is because the wind could be so dense that it blocks the photons from the star in such a way that they cannot reach the disk. Therefore, the disk cannot be sufficiently ionized to wind launching conditions. However, in our wind models we ignore this effect because there are other ways to ionize the disk and our disk is already very thin. Thus, we assume full disk ionization and a disk wind that extends the entire length of the disk. This was also motivated by the fact that the x-wind is a very compact outflow, so to cast a wide-spread parameter net, we decided that a fully extended disk wind would be most beneficial.

Chapter III: Methodology

Monte Carlo Radiative Transfer

To simulate our models, we used a Monte Carlo Radiative Transfer (MCRT) code previously constructed to model the outflows of a protostellar system. MCRT is a statistical approach to modeling photon propagation. The foundation of MCRT is the use of random number probability distributions to determine the scattering or absorption events of a photon packet in a

particular zone of the modeled system. (*See Appendix B of Bans et al., 2012 for an in-depth description of the MCRT scheme used in this project*).

The Spectral Energy Distribution

A number of photon packets of different wavelengths sampled from a blackbody distribution based on the star's temperature leave the star at random angles. The photon packets can then travel through the wind. Once within the wind, the grain opacities as well as the densities and temperatures of the grains set how likely the photon packet of a certain wavelength is to experience a scattering or absorption event in a zone of the wind. When a photon packet is absorbed, it is subsequently reemitted at a different wavelength. Due to conservation of energy, the absorption event heats the zone within which it occurs and changes the properties of the wind zone for future events. After many packets, the process reaches a stable temperature equilibrium. A scattering event does not change the temperature of the zone, but instead changes the angle at which the photon packet is traveling. Eventually the photon packets, which could have different wavelengths from various absorption events, leave the wind at different angles. The spectral energy distribution is ultimately calculated by the number of photons in different wavelength bands that leave the wind at each possible angle.

Binning and Zoning

The simulated disk winds and x-winds were zoned according to the geometry of the system. The disk wind is broken up into 100 vertical and horizontal zones, where the horizontal zones are spaced out logarithmically. In the x-wind case, we only fit 10 streamlines from Shu et al. (1997), thus the x-wind was zoned with 100 vertical zones and 9 horizontal zones. As the photon packets leave the system, they are binned according to wavelength and inclination in order to construct the spectral energy distribution. Thus, the number of sampled photons (described in the resolution

section below) is naturally divided into these bins. We chose to run most models using 1024 wavelength bins. However, in the cases of less computationally expensive simulations, we sorted escaped packet energies into smaller wavelength bins so that we could have more data points on our SED plots.

Resolution

Due to the statistical nature of the MCRT code, it requires a large number of photon packets for precision. However, this can become very computationally expensive. In the MCRT code used in this project, there was no artificial limit to the number of scattering or absorption events a photon packet could experience within a particular zone. Many of our models involved compact winds with very high optical depths due to high mass or narrow width (*See Tables A.1, A.2, and A.3*). For these models, packet events can take a very long time and in return increase the simulation run time. Thus, for some simulations we needed to reduce the number of sampled packets. In the future we plan to investigate if we can limit the number of a single packet's events in the wind to speed up the computation time without compromising on an accurate description of the packet's changing energy. (*See Figure 12 for the effect of reduced photon packets on the resultant SED plot)*.

As our project is primarily a proof of concept for novel outflow geometries, our analysis of results was qualitative (*See Chapter IV for Results*). If we were to quantitatively find the best fit models for each geometry, we would need to keep the binning and photon packet sampling consistent (*See Chapter VI for future directions*).

As the MCRT code we used was originally built for the protostellar case, we had to adapt the structure of the code for the white dwarf system. This means that we tested the code for the smaller geometries of the system and had to adjust precision calculations accordingly. We

increased the spatial precision in parts of the code that had to integrate along the white dwarf system parameters to stay consistent with the new smaller zoning sizes.

Disk Models

In our simulations we used two types of disks, the regular disk and the active disk. The regular disk is treated as a two-component flat disk model as used in Bans et al. (2012). The top half of the disk is an auto-absorption layer. This means that instead of utilizing a probability distribution to determine the event of the photon as it interacts with the disk, the photon is instead automatically absorbed by the disk and reemitted at a new wavelength. Half of the reemitted photons from the top half of the disk travel into the interior layer of the disk. The interior layer radiates as a pure blackbody.

In the case of low masses, the disk may no longer be optically thick enough to hold the blackbody assumption true. Therefore, we developed an active disk model for the low mass disk-wind simulations. The active disk model treats the entire disk like the wind, meaning that it is zoned accordingly and that a random probability distribution is used to determine the photon scattering or absorption event. The photons contributing to the overall spectral energy distribution could have experienced many events within the disk, which in the optically thin case would be more accurately calculated by the active disk model. To construct the most representative spectral energy distribution, we used the active disk when simulating the 1-asteroid, 3-asteroid, and 5-asteroid mass disk-wind models.

Chapter IV: Results

The following results show the spectral energy distribution for G29-38 in each modeled system. The simulated spectral energy distribution is normalized to the blackbody curve for G29-38. Qualitatively, a good fit for the SED means i) the flux at 10 microns should match the flux at

~1 micron and ii) the SED should have a smaller peak in the 2-3 micron range (NIR) than it does around 10 microns. The Infrared spectroscopic data and IRAC observational data from the *Spitzer Space Telescope* as well as the observational data from the 2MASS survey for G29-38 are shown in each plot. Inclination angles for G29-38 have been found through various fittings to be between 55° and 65°, however these results were not considered reliably precise and instead were used to constrain the inclination angles away from the edge-on and face-on options (Montgomery et. al, 2005; Thompson et al., 2010). Therefore, all of the spectral energy distributions besides those in *Figure 16* are plotted at an inclination of 40 degrees.

For the asteroid disk wind models, the 10-micron emission was present under all parameters, but depending on the mass of the model, the flux was under produced (*See Figure 5*). The 3-asteroid mass and the 5-asteroid mass models showed a good fit to the observed flux for the 10-micron feature. However, in these models the NIR excess emission was nonexistent. In the 1 asteroid mass models parameterized by the upper limit of the magnetic field, the NIR excess feature began to take shape, but the flux levels were much too small.

The Earth disk wind models produced the 10-micron feature but at a flux level much too high (*See Figure 6*). The NIR flux decreased for models further from the star than the models closer to the star. This makes sense physically, because the NIR excess emission requires hotter dust temperatures. However, in the 3 Earths mass disk wind models compared to the 1 Earth mass disk wind models, the NIR excess emission remained present and at a comparable flux to the 10-micron feature as the models increased their distance from the star. This would suggest that in these cases the mass may be more important than the magnetic truncation radius when recreating the NIR emission feature. However, the 3 Earths mass model with a magnetic field of 20 kG and a truncation coefficient of 1 reveals a drop in the NIR excess emission when compared to the other

3 Earths mass models. This implies that there is some limiting distance away from the star at which the temperatures are too low for the NIR excess feature. In the 5 Earths mass disk wind models, the NIR emission was over produced in models with closer winds to the star and under produced in models with further winds from the star. Therefore, the NIR emission feature is dependent not just on mass and the magnetic truncation radius, but also on the density of the wind as the width of the wind changes between the 1 Earth, 3 Earths, and 5 Earths mass disk wind models (e.g. the 5 Earth mass disk-wind models had a narrower wind extent, assuming a disk scaling of 5 x R_L – see *Table A.1* for all explicit model parameters).

In the Jupiter-mass disk wind models (*see Figure 7*), the flux of the 10-micron feature is again over produced, but not as much as in some of the Earth models. This is perplexing, as one would assume that more dust would lead to more overproduced spectral signatures. However, it is possible that the first few field lines of the disk wind are so dense that they effectively shield the rest of the field lines behind them from interacting with the photons. It is also possible that the wind extent could affect these models because although the Roche limits are comparable for the Earth mass and Jupiter mass models, some of the Earth mass and Jupiter mass models required a disk scaled to $10R_L$ or even $11R_L$ (*see Table A.1 for details*). Finally, photon packet resolution effects could be influencing the SED plots of the Jupiter-mass models because even though photon resolutions don't affect the overall flux levels (*see Figure 12*), the lack of resolution in the high mass Jupiter plots could distort our qualitative analysis of the flux.

We also find in the 1-Jupiter mass models and the 3 Jupiter mass models under the upper magnetic field parameter that the relative strengths of the NIR excess and 10-micron silicate feature are most comparable to the observed SED of G29-38 (though all the IR emission from the dust is too strong compared to the stellar emission). This is interesting because the 5 Earth mass

models under the upper limit magnetic field parameter over produced the 10-micron feature. These results further imply that the limiting factor for the best fit to the SED cannot just be wind mass or wind placement, but also wind density. To explore this further, we analyzed the optical depths of the wind.

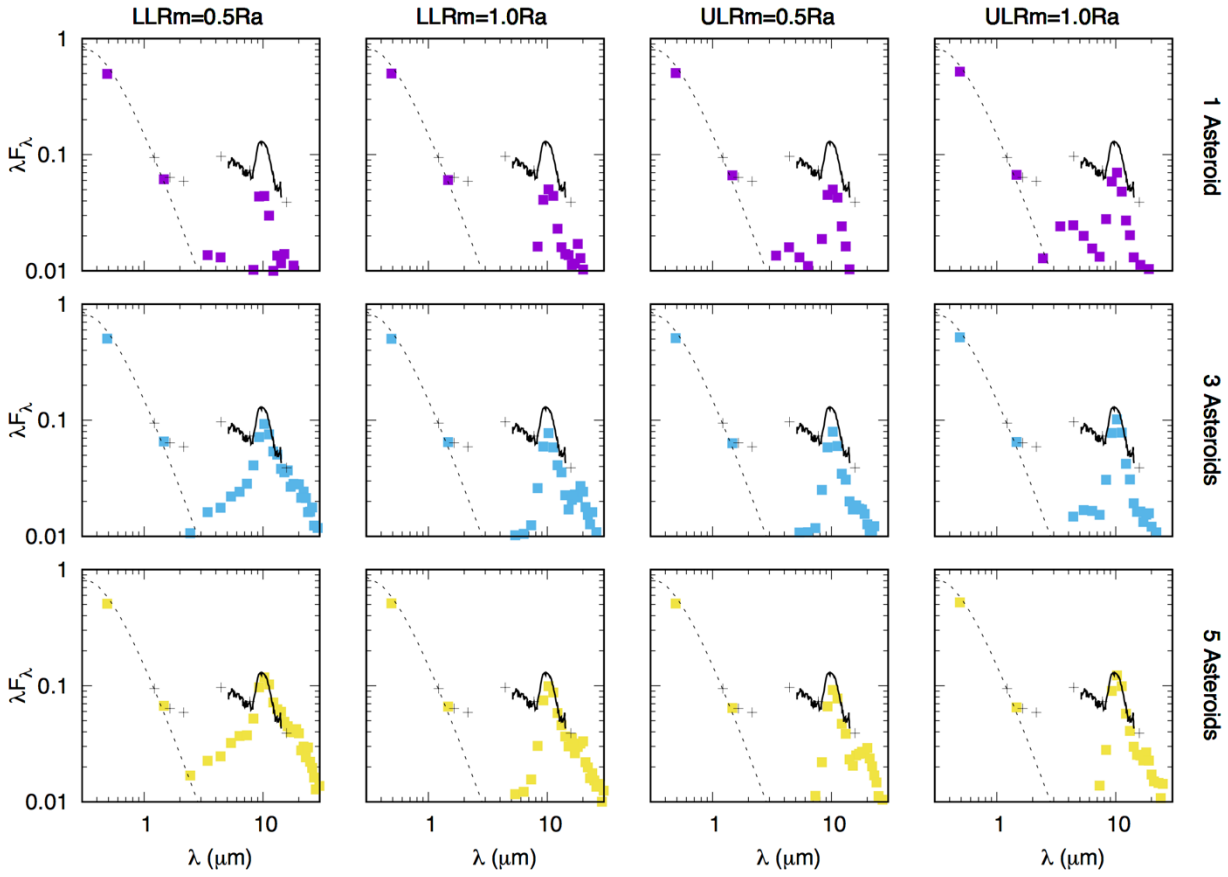

Figure 5. The following plot shows the spectral energy distribution normalized to the 11,800K blackbody curve for the 12 disk wind models with asteroid-like masses. These simulations were run with the active disk model. All SED plots are shown at a 40-degree inclination. The first row shows the SED plots (purple) of a 1 asteroid mass disk and a 1/100th asteroid mass wind for the four different magnetic truncation radii calculated according to the "LL" or the lower limit magnetic field, 2.5 kG, and the "UL" or upper limit magnetic field, 20 kG with either the Alfven radius coefficient value of $\xi = 0.5$ or $\xi = 1$. The observations of G29-38 are plotted from the *Spitzer Space Telescope* Infrared spectrograph (solid black line), the *Spitzer Space Telescope* IRAC data (points closest to 1, 2, and 3 microns), and the 2MASS survey data (the points closest to the solid black line). The second row shows the SED plots (blue) for the 3-asteroid disk mass and the 1/100th of 3 asteroids wind mass models under the four different magnetic truncation radii parameters. The third row shows the SED plots (yellow) for the 5-asteroid disk mass and the 1/100th of 5 asteroids wind mass modeled under the different truncation parameters.

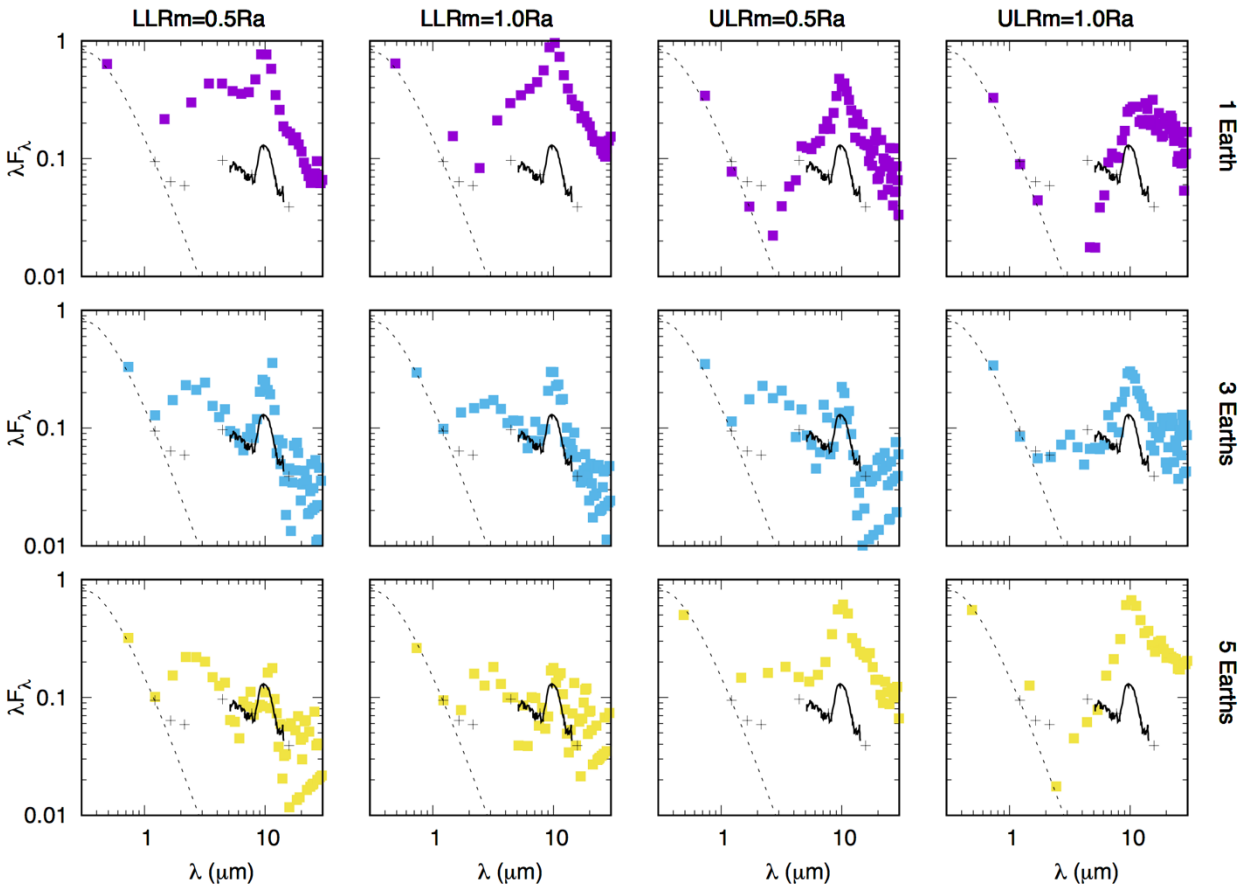

Figure 6. The following plot shows the spectral energy distribution normalized to the 11,800K blackbody curve for the 12 disk wind models with Earth-like masses. Every SED plot is shown at 40-degree inclination. The first row shows the SED plots (purple) of a 1 Earth mass disk and a 1/100th Earth mass wind for the four different magnetic truncation radii calculated according to the "LL" or the lower limit magnetic field, 2.5 kG, and the "UL" or upper limit magnetic field, 20 kG and depending on the coefficient value $\xi = 0.5$ or $\xi = 1$. The observations of G29-38 are shown from the *Spitzer Space Telescope* Infrared spectrograph (solid black line), the *Spitzer Space Telescope* IRAC data (points closest to 1, 2, and 3 microns), and the 2MASS survey data (the points closest to the solid black line). The second row shows the SED plots (blue) for the 3 Earth disk mass and the 1/100th of 3 Earth wind mass models with the four different magnetic truncation radii. The third row shows the SED plots (yellow) for the 5 Earth disk mass and the 1/100th of 5 Earths wind mass modeled with the four different magnetic truncation radii parameters. The middle two plots of the second row and the first two plots of the third row show some messy points and some "line like" features past 10 microns. This indicates that not enough photon packets were sampled to fully resolve the SED plot (*See Figure 12 for further discussion of photon resolution effects).*

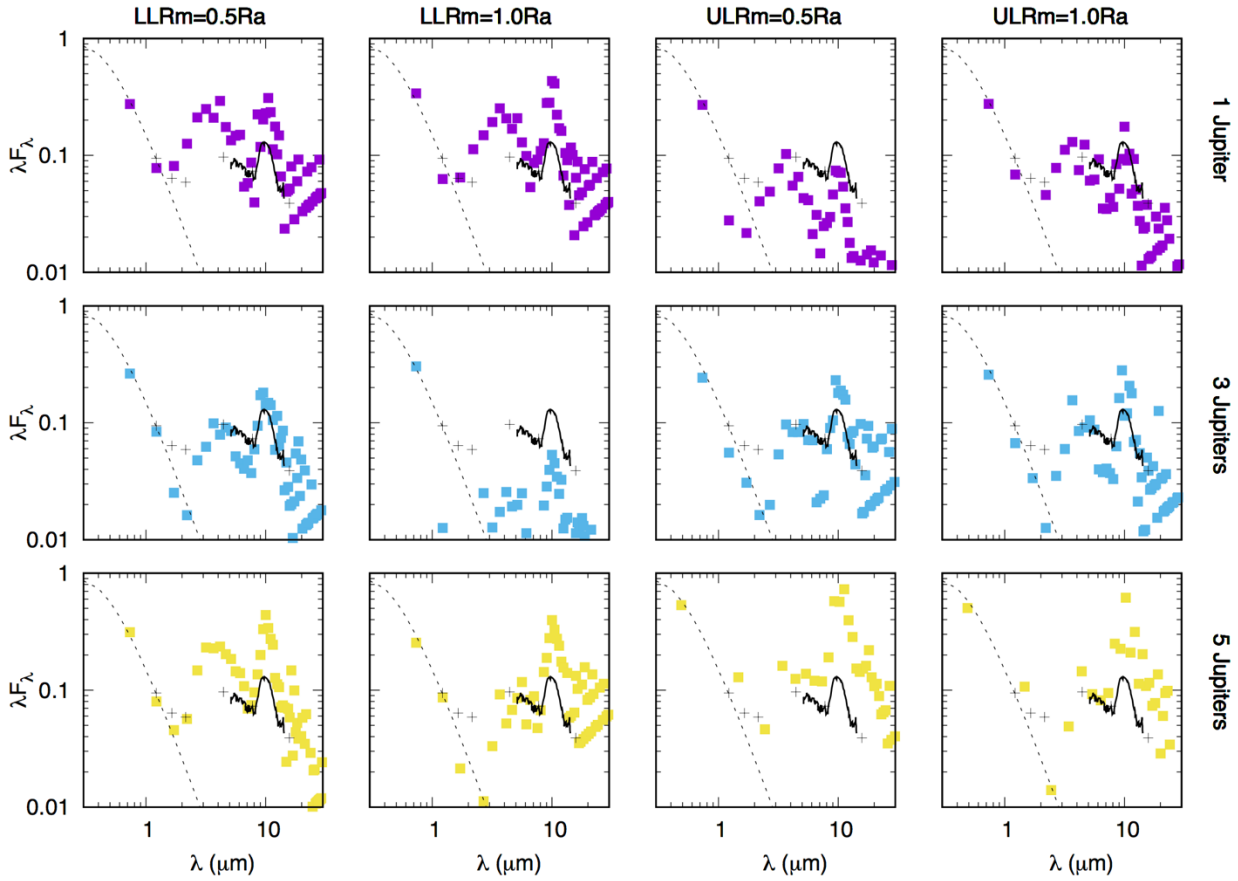

Figure 7. The following plot shows the spectral energy distribution normalized to the 11,800K blackbody curve for the 12 Jupiter (x1, x3, x5) mass disk wind models. Every SED plot is shown at 40-degree inclination. The first row shows the SED plots (purple) of a 1 Jupiter mass disk and a 1/100th Jupiter mass wind for the four different magnetic truncation radii calculated according to the "LL" or the lower limit magnetic field, 2.5 kG, and the "UL" or upper limit magnetic field, 20 kG and depending on the coefficient value $\xi = 0.5$ or $\xi = 1$. The observations of G29-38 are shown from the *Spitzer Space Telescope* Infrared spectrograph (solid black line), the *Spitzer Space Telescope* IRAC data (points closest to 1, 2, and 3 microns), and the 2MASS survey data (the points closest to the solid black line). The second row shows the SED plots (blue) for the 3 Jupiter disk mass and the 1/100th of 3 Jupiter mass wind models with the four different magnetic truncation radii. The third row shows the SED plots (yellow) for the 5 Jupiter disk mass and the 1/100th of 5 Jupiters mass wind modeled with the four different magnetic truncation radii parameters. Some of these SED plots show some messy points and some "line like" features past 10 microns. This indicates that not enough photon packets were sampled to fully resolve the SED plot (*See Figure 12 for further discussion of photon resolution effects).*

We calculated the optical depths through the base of the wind for every simulated disk wind model (*See Table A.2*). The code calculates the optical depth for a 500 nm photon and for an FUV photon. To get the optical depth for a photon with a wavelength comparable to the temperature of the wind, we took the average of the two optical depths. The wind decreases in density with height and with radial distance. Therefore, the optical depths through the base of the wind can be considered the maximum optical depth for the wind. The optical depths increase as we would expect, with a positive correlation to the increase in model mass. Yet within each mass option (e.g. 1 Earth mass) there are extreme differences between the optical depths of the various wind extents, which indicate a dependency of optical depth on density.

We see the role of wind density in the fit of the SED more clearly in the x-wind model results. The SED plots from the asteroid-mass x-wind models don't vary too much from the disk wind results (*See Figure 8)*. This is interesting because x-winds are launched from a much narrower point in the disk, resulting in a much more compact wind. The optical depths through the base of the x-wind models, on average, are about 0.001 of the optical depths in the disk winds cases due to their narrow launch extent (*See Table A.3*).

However, when we transition our models from asteroid masses to Earth masses, there is a large increase in the SED flux (*See Figure 9)*. Across the Earth mass x-wind models, the NIR excess is hardly present while the 10-micron feature is extremely overproduced. In the Jupiter mass x-wind models, again the flux is overproduced (*See Figure 10)*. It is likely that the x-wind model is overproducing the flux in the Earth and Jupiter mass models because the density of the x-wind doesn't decrease as steeply with vertical height as the density of the disk-winds (*See Figure 11)*. However, unlike the Earth mass x-winds, the Jupiter mass models show the NIR excess emission feature with the correct relative flux to the 10-micron feature, even though the flux is

much higher than that of the star. This is again perplexing, but it does imply that though the amount of dust within these models is too high, there is some balance of parameters that can recreate the NIR emission and 10-micron shape simultaneously.

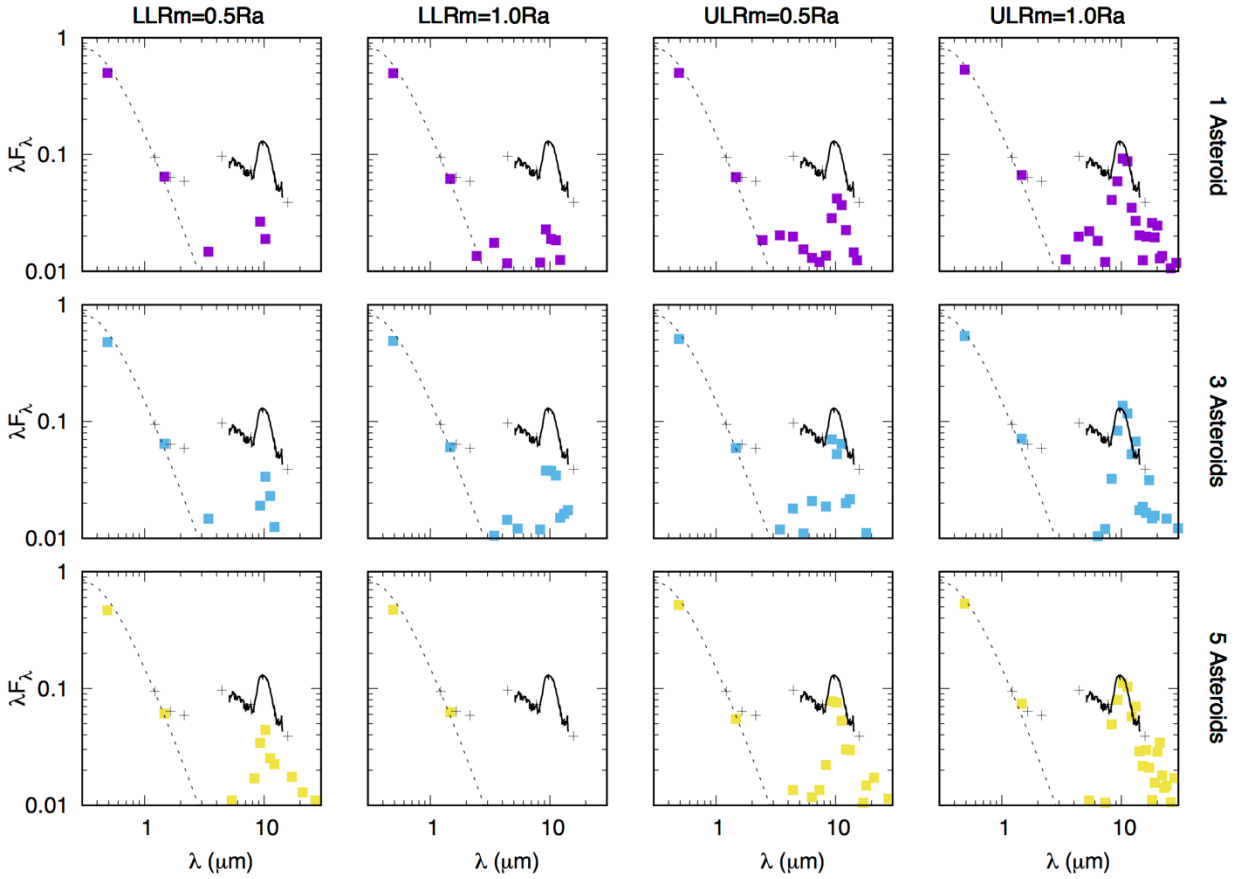

Figure 8. The following plot shows the spectral energy distribution normalized to the 11,800K blackbody curve for 12 asteroid mass x-wind models. Every SED plot is shown at 40-degree inclination. The first row shows the SED plots (purple) of a 1 asteroid mass disk and a 1/100th asteroid mass wind for the four different magnetic truncation radii calculated according to the "LL" or the lower limit magnetic field, 2.5 kG, and the "UL" or upper limit magnetic field, 20 kG and depending on the coefficient value $\xi = 0.5$ or $\xi = 1$. The observations of G29-38 are shown from the *Spitzer Space Telescope* Infrared spectrograph (solid black line), the *Spitzer Space Telescope* IRAC data (points closest to 1, 2, and 3 microns), and the 2MASS survey data (the points closest to the solid black line). The second row shows the SED plots (blue) for the 3-asteroid disk mass and the 1/100th of 3 asteroids wind mass modeled with the four different magnetic truncation radii. The third row shows the SED plots (yellow) for the 5-asteroid disk mass and the 1/100th of 5 asteroids wind mass modeled with the four different magnetic truncation radii parameters.

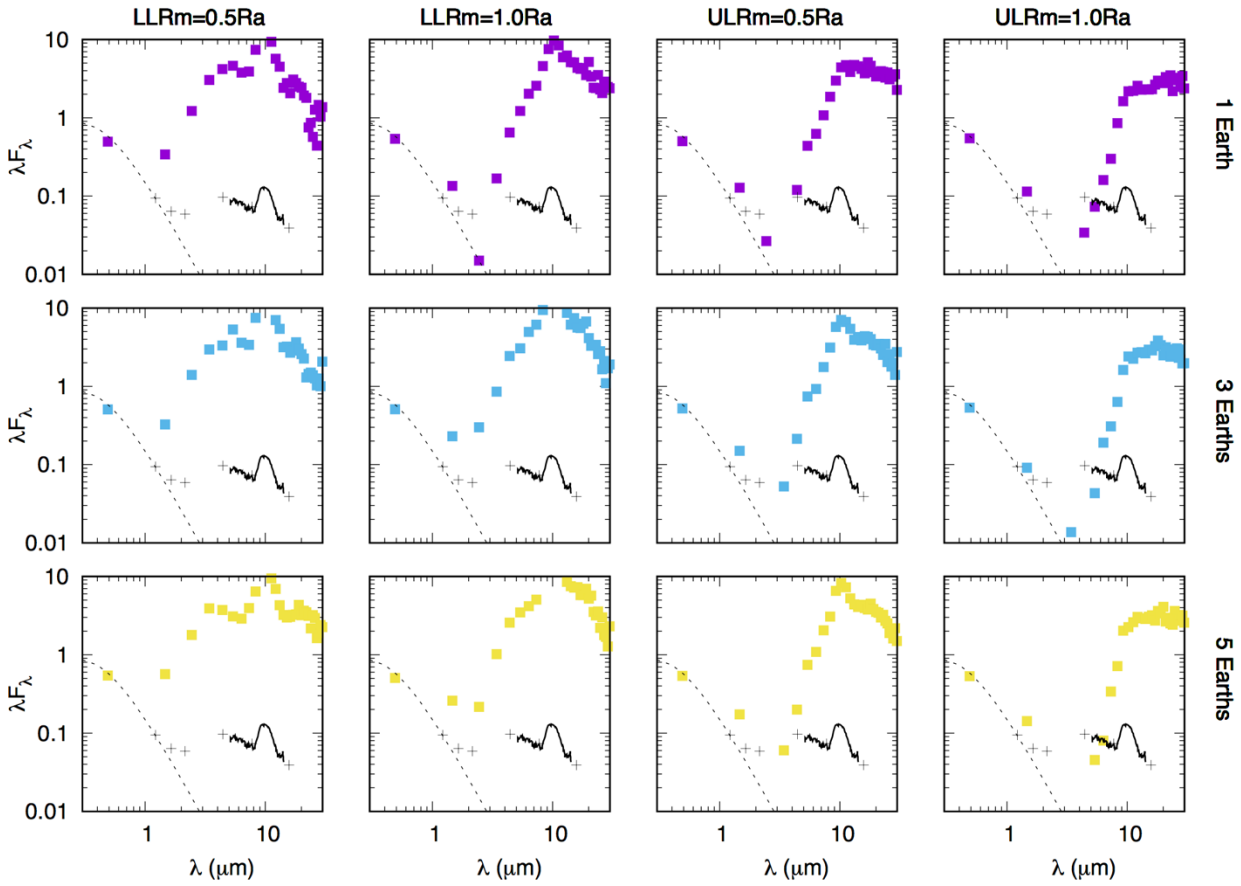

Figure 9. The following plot shows the spectral energy distribution normalized to the 11,800K blackbody curve for 12 Earth mass models. Every SED plot is shown at 40-degree inclination. The first row shows the SED plots (purple) of a 1 Earth mass disk and a 1/100th Earth mass wind for the four different magnetic truncation radii calculated according to the "LL" or the lower limit magnetic field, 2.5 kG, and the "UL" or upper limit magnetic field, 20 kG and depending on the coefficient value $\xi = 0.5$ or $\xi = 1$. The observations of G29-38 are shown from the *Spitzer Space Telescope* Infrared spectrograph (solid black line), the *Spitzer Space Telescope* IRAC data (points closest to 1, 2, and 3 microns), and the 2MASS survey data (the points closest to the solid black line). The second row shows the SED plots (blue) for the 3-Earth disk mass and the 1/100th of 3 Earth wind mass modeled with the four different magnetic truncation radii. The third row shows the SED plots (yellow) for the 5 Earth disk mass and the 1/100th of 5 Earth wind mass modeled with the four different magnetic truncation radii parameters.

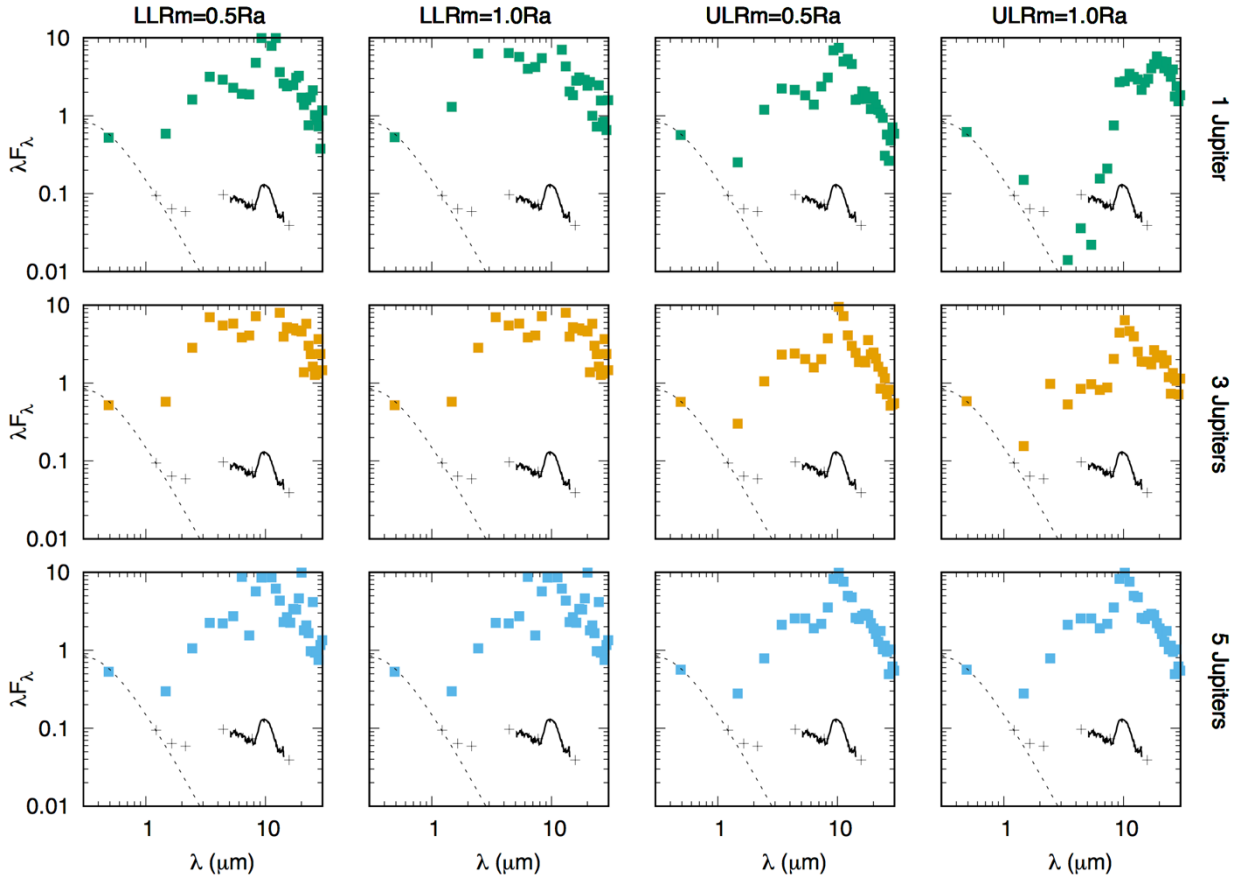

Figure 10. The following plot shows the spectral energy distribution normalized to the 11,800K blackbody curve for 12 Jupiter mass x-wind models. The SED plots are shown at a 40-degree inclination. The first row shows the SED plots (purple) of a 1 Jupiter mass disk and a 1/100th Jupiter mass wind for the four different magnetic truncation radii calculated according to the "LL" or the lower limit magnetic field, 2.5 kG, and the "UL" or upper limit magnetic field, 20 kG and depending on the coefficient value $\xi = 0.5$ or $\xi = 1$. The observations of G29-38 are shown from the *Spitzer Space Telescope* Infrared spectrograph (solid black line), the *Spitzer Space Telescope* IRAC data (points closest to 1, 2, and 3 microns), and the 2MASS survey data (the points closest to the solid black line). The second row shows the SED plots (blue) for the 3 Jupiter disk mass and the 1/100th of 3 Jupiter wind mass modeled with the four different magnetic truncation radii. The third row shows the SED plots (yellow) for the 5 Jupiter disk mass and the 1/100th of 5 asteroids wind mass modeled with the four different magnetic truncation radii parameters.

The optical depths through the base of the x-wind and disk wind models are very different. One would think that the greater the flux is over produced, the greater the optical depth of the model. However, that is not the case when comparing the flux differences in the disk wind models and the x-wind models. But, the density distribution profiles through the x-wind and disk wind are also very different. We investigated the density distribution of a high mass wind model (e.g. a 3 Jupiter mass model with $\xi = 1$ and magnetic field 2.5 kG) that under produced the SED flux in the disk wind model and over produced the flux in the x-wind model. The density distribution of the disk wind drops much quicker than the density distribution of the x-wind (*See Figure 11*).

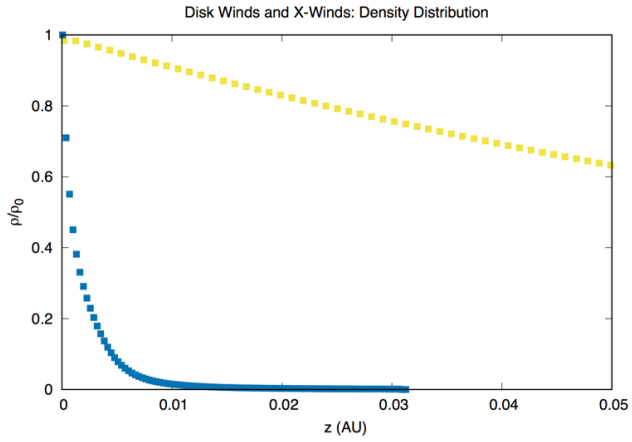

Figure 11. The normalized density distributions for a disk wind (blue) model and an x-wind (yellow) model are plotted in AU along the x-axis for a 3 Jupiter mass system, in the lower magnetic field limit, with a coefficient of $\xi = 1$ and a magnetic field of 2.5 kG

The density distribution of the x-wind means that as the x-wind outflow extends further away from the sun and cools down, it still has more than enough dust to intercept the cooler stellar radiation. Therefore, the x-wind model would produce a much higher 10-micron feature than the disk wind model. However, the x-wind models have a difficult time reproducing the NIR excess feature.

As mentioned in Chapter III, the photon packet sampling differed for each of the simulated models. We investigated the effects of photon packet resolution on the spectral energy distribution (*See Figure 12)* and while increased packet resolution produces a sharper peak for the 10-micron feature and a more resolved general shape, it does not change the overall flux production. When the packet resolutions are too low in our models, it can result in noisier SED plots that have artificial lines at wavelengths greater than 10 microns that are a result of single photons binning at those wavelengths.

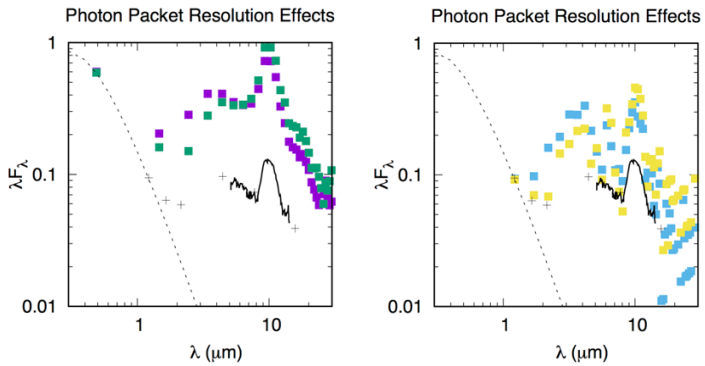

Figure 12. These are SED plots for (on the left-hand side) 1 Earth disk wind system in the lower limit of 2.5 kG with ξ = 1. These parameters are plotted with 1 million photon packets (green) and with 500,000 photon packets (purple) and for (on the right-hand side) 1 Jupiter disk wind system in the upper limit of 20 kG with ξ = 0.5. These parameters are plotted with 50,000 photon packets (light blue) and 25,000 photon packets (yellow). The 50,000 and 25,000 photon packets produce a less resolved SED plot and create artificial lines at higher wavelengths.

From these results, it is clear that wind type, wind density distribution, mass, and width of wind heavily affected the modeled SED outcome. Wind width is directly related to wind type and the relationship between the magnetic truncation radius and the Alfven radius. We chose one example for the Asteroid masses, Earth masses, and Jupiter masses disk wind models and compared the SED plots to their corresponding x-wind model to explore how these parameters affected the SED plots for the modeled systems (*See Figure 13)*. The first models we chose were the 1 asteroid mass, 20 kG, $\xi = 1$, 5 Earth mass, 2.5 kG, $\xi = 1$, and the 1 Jupiter mass, 20 kG, $\xi = 0.5$.

These three disk wind models had very different parameters (*See Table 4*). They were launched from different points away from the star and their wind widths varied greatly. The inner radius for the 1 Asteroid model was much further away from G29-38 than the 5 Earths and 1 Jupiter model (*See Figure 14*). This may be the reason that despite similar fluxes across all three models for the 10-micron feature, the 1 Asteroid model under produces the 2-3 micron emission feature. For the 1 Asteroid model, its disk wind may start too far from the star and is therefore too cold for the NIR excess.

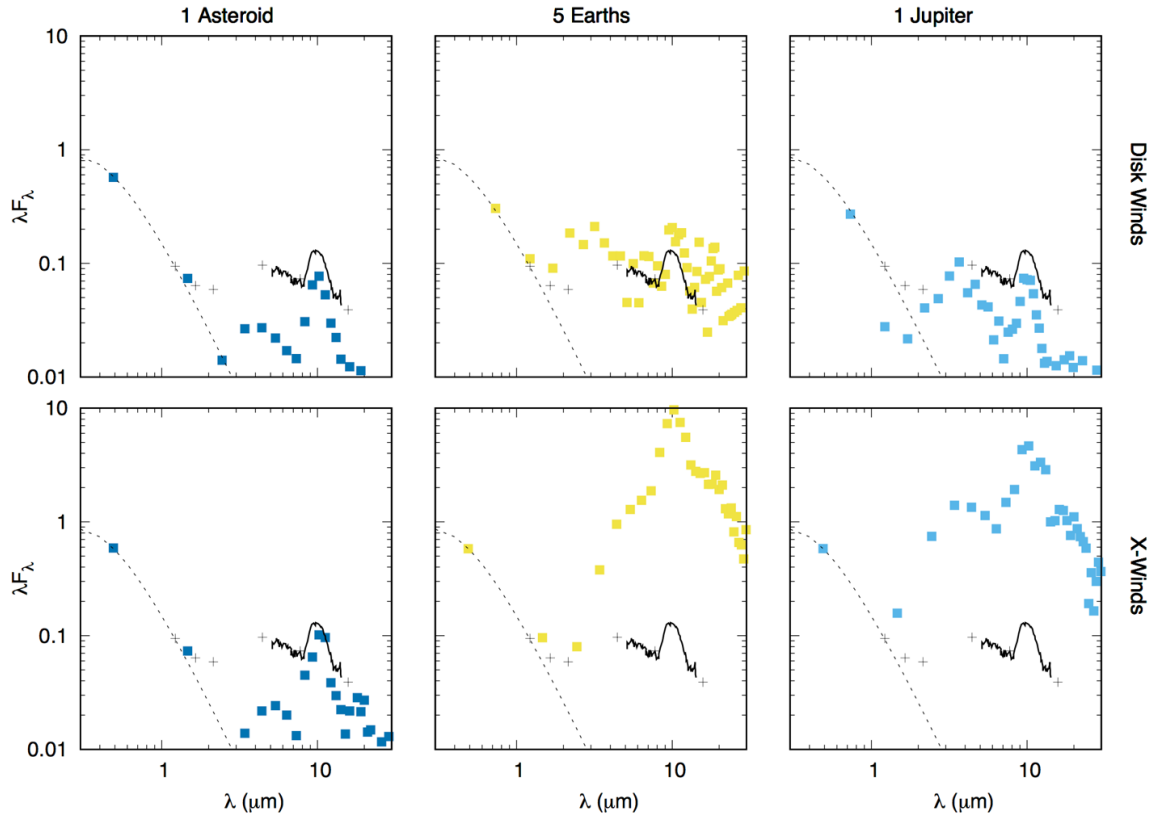

Figure 13. The SED for a 1/100th 1 asteroid mass wind in a 20 kG system, $\xi = 1$ is shown (red) for a disk wind and an x-wind under identical parameters. The SED for a 1/100th 5 Earths mass wind in a 2.5 kG system, $\xi = 1$, is shown (yellow) for a disk wind and x-wind under identical parameters. Though the flux is comparable to the observed SED, the simulated disk wind data is not very resolved due to low packet numbers sampled. The SED for a 1/100th 1 Jupiter mass wind in a 20 kG system, $\xi = 0.5$ is shown (blue) for a disk wind and x-wind under identical parameters. The x-wind data is also normalized to the black body curve.

Object	Disk Mass	Wind Mass	B	ξ	R_{inner} (cm)	R_{outer} (cm)	Wind Width (cm)
1 Asteroid	8.276×10^{22}	8.276×10^{20}	20	1	3.088×10^{11}	3.833×10^{11}	7.455×10^{10}
5 Earths	1.792×10^{28}	1.792×10^{26}	2.5	1	9.411×10^{10}	1.543×10^{11}	6.0224×10^{10}
1 Jupiter	1.898×10^{30}	1.898×10^{28}	20	0.5	1.544×10^{11}	4.332×10^{11}	2.7884×10^{11}

Table 4. The parameters for the three disk-wind models. B is the magnetic field magnitude in kG.

Though the 10-micron fluxes are close in magnitude, the 5 Earth mass model produces more flux that the Jupiter mass. The width of the wind of the 1 Jupiter model is much greater than the 5 Earths model. Perhaps the lower flux levels are due to the density decrease in an extended wind such as that for the 1 Jupiter model. Yet, the mass of the wind for the Jupiter model is orders of magnitude larger than the 5 Earths and 1 Asteroid model, so while the wind is more spread out, it could still have a comparable density. To explore this further, we plotted the density distributions for the disk wind models and their corresponding x-wind models, as well as the field line shapes (*See Figure 15*).

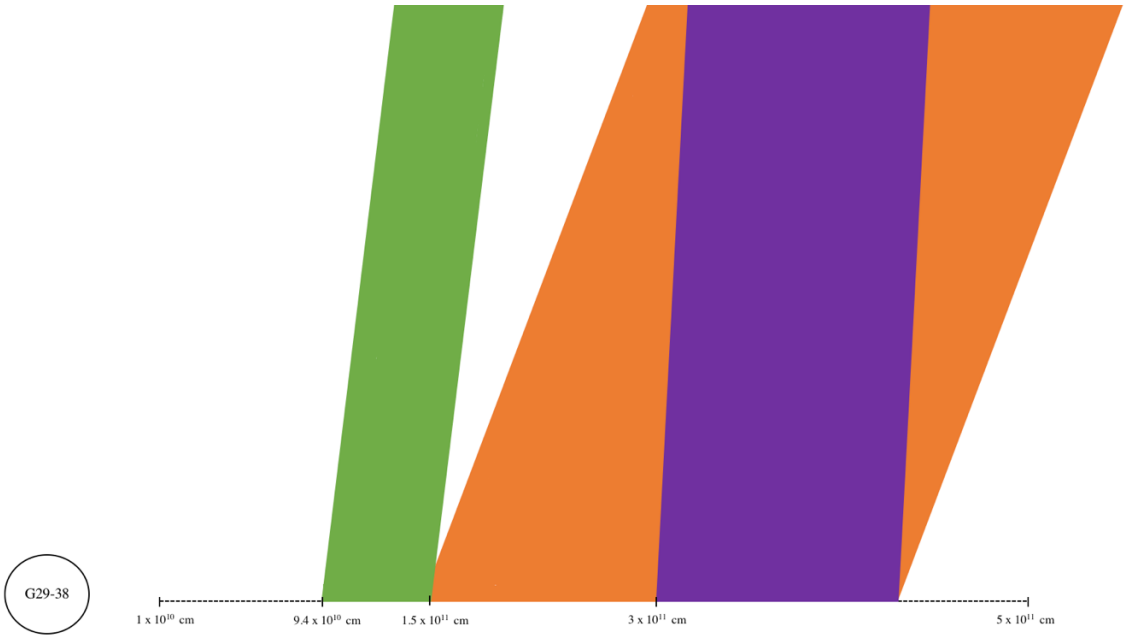

Figure 14. Here a schematic representing the different wind launching points, launching angles, and wind widths for the three models above. 5 Earths (green), 1 Jupiter (orange), and 1 Asteroid (purple). The 1 Asteroid wind launches at the half way point for the 1 Jupiter wind.

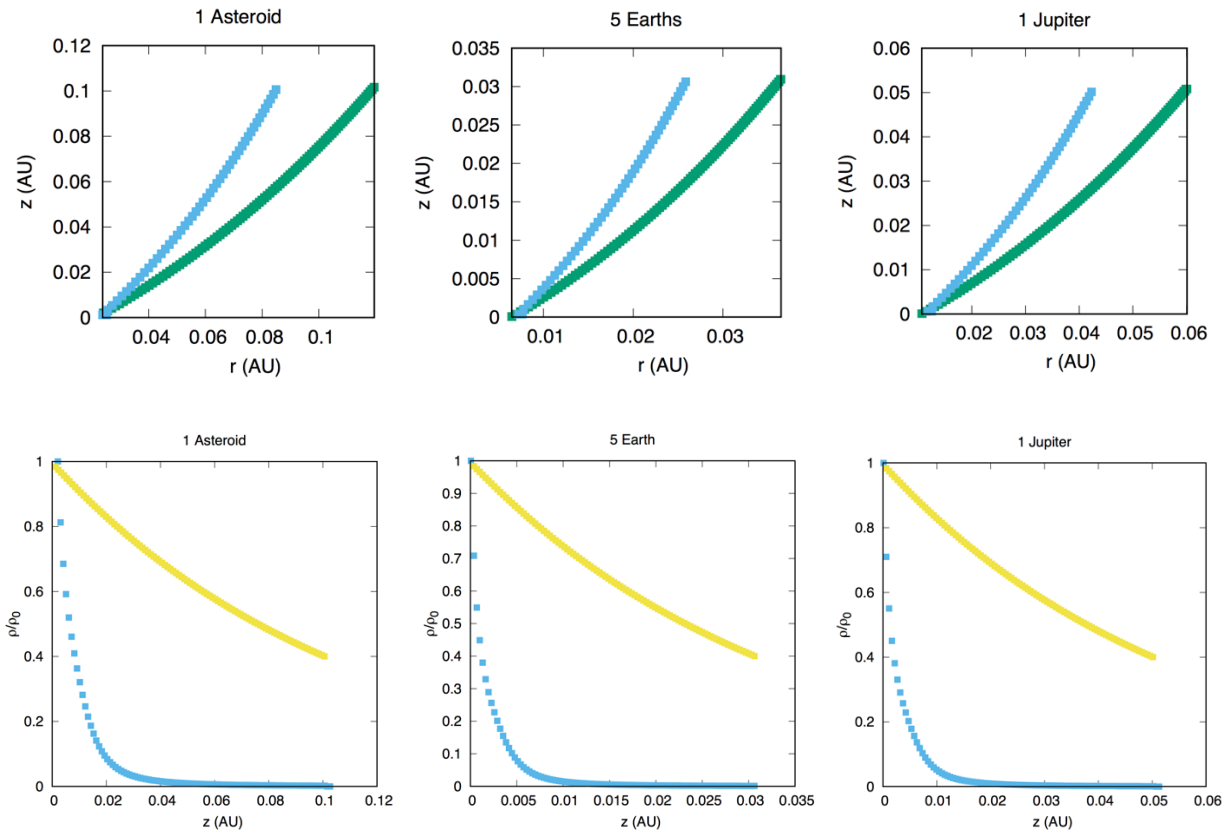

Figure 15. The top row of plots shows (from left to right) the field line shapes for the 1 Asteroid mass, 5 Earths mass, and 1 Jupiter mass models. The disk wind model is plotted in green and the x-wind model is plotted in blue. The bottom row of plots shows (from left to right) the density distribution of the outflows for the 1 Asteroid mass, 5 Earths mass, and 1 Jupiter mass models. The disk wind is plotted in blue and the x-wind model is plotted in yellow.

As seen previously (*see Figure 11*), the density profile decreases much faster for a disk wind outflow than for an x-wind outflow. We scaled the starting density at the base of the innermost streamline such that the total mass matched our chosen masses of the disk and wind system. The overall shape and distribution of the wind is set by the wind model type (disk-wind models C, E, or G, or the x-wind model). Initially we chose disk wind model type C for its vertical height and ability to capture starlight. Yet the field line shape for disk wind model type C is less vertical than the field line shape for the x-wind. Therefore, the x-wind model should be able to capture the most starlight of the system. That fact, along with its slowly decreasing vertical density distribution, is why our x-wind model can produce so much IR flux. Of course, the amount of

starlight that is forced to be captured by the wind is also strongly dependent on the inclination angle of the system. Therefore, it is important to examine closer the inclination effects on the modeled systems.

We chose the models with the least amount of photon resolution effects to demonstrate how inclination affects the spectral energy distribution. We plotted the following models: 1 asteroid mass, 20 kG, ξ = 1, 5 Earth mass, 20 kG, ξ = 0.5, and the 1 Jupiter mass, 20 kG, ξ = 0.5 for both the disk-wind model and the x-wind model to examine the inclination effects of 30 degrees, 40 degrees, 50 degrees, and 60 degrees on the fit of the system (*See Figure 16*).

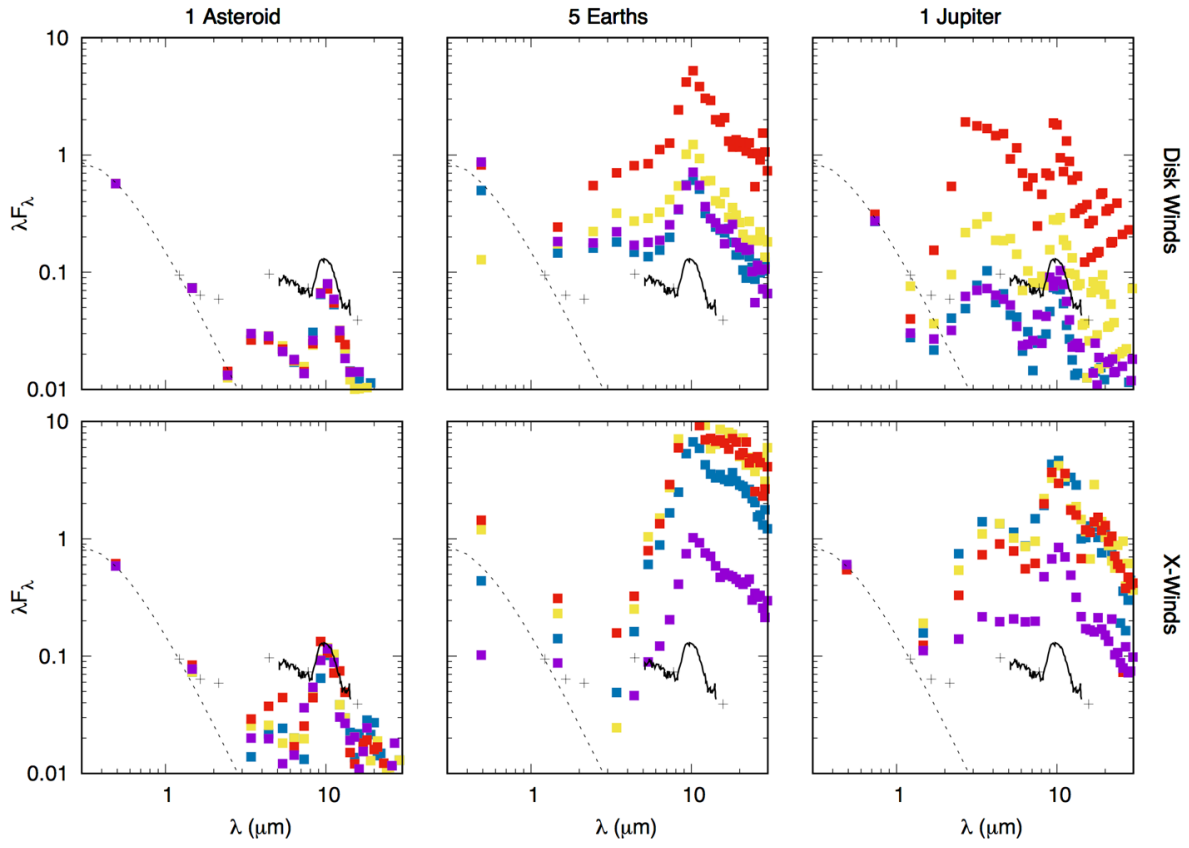

Figure 16. The spectral energy distributions of the 1 asteroid mass, 20 kG, ξ = 1, 5 Earth mass, 20 kG, ξ = 0.5, and the 1 Jupiter mass, 20 kG, ξ = 0.5 disk wind models and x-wind models are plotted at 30 degrees (purple), 40 degrees (blue), 50 degrees (yellow), and 60 degrees (red).

In the asteroid model the inclination angles don't affect the overall shape and flux levels of the SED. However, it is clear that inclination angle has a large effect on the fit of the spectral energy distribution in the higher mass models.

Chapter V. Discussion

Angle of Inclination

The toy models we constructed for the disk and x-winds can tell us something physical about the system when we investigate the angle of the outflow. In all models, the height of the wind was scaled to 5 times the magnetic truncation radius. Therefore, if we use the width of the wind and the height of the wind, we can determine the launching angle of the wind with respect to the accretion disk (*See Table A.4*). In all of the wind models, the angle of the wind with respect to the start of the accretion disk is about the same, therefore the inclination effects seen in *Figure 16* require closer study.

The key components to understanding the inclination effects on the SED plots between 30° and 60° is the width and density distribution of the outflow. The 0-degree inclination angle is generally considered as the "face on" angle that directly looks at the star and sees the wind from the top down. The 90-degree inclination angle is considered to be "edge on", which looks along the disk and doesn't directly see the star. At different inclination angles, it is possible to get starlight that hasn't passed through a lot of wind. At lower inclination angles, a greater portion of starlight can be observed that hasn't been forced to travel through the dusty outflow (*See Figure 17*).

If we plotted the SEDs for a face-on, 0 degrees scenario, (or a 10° or 20° scenario) we would see a higher amount of starlight that hasn't traveled through the outflow, which would result in a higher flux from the stellar blackbody component and thus a comparatively lower flux in the

IR. While light from the star in all the inclinations explored in *Figure 16* would be forced to travel through the wind, the difference in the SED plots for the various inclination angles ultimately boils down to where the direct path of the starlight would intercept the wind. The higher up along the outflow that the starlight penetrates, the less dense the outflow will be, and the starlight will be more likely to escape without any interactions with the wind. This follows well with *Figure 16*, as the 60-degree inclination angle (plotted in red) shows a larger IR flux than the 30-degree inclination angle (plotted in purple) in the Jupiter and Earth cases for both disk-wind models.

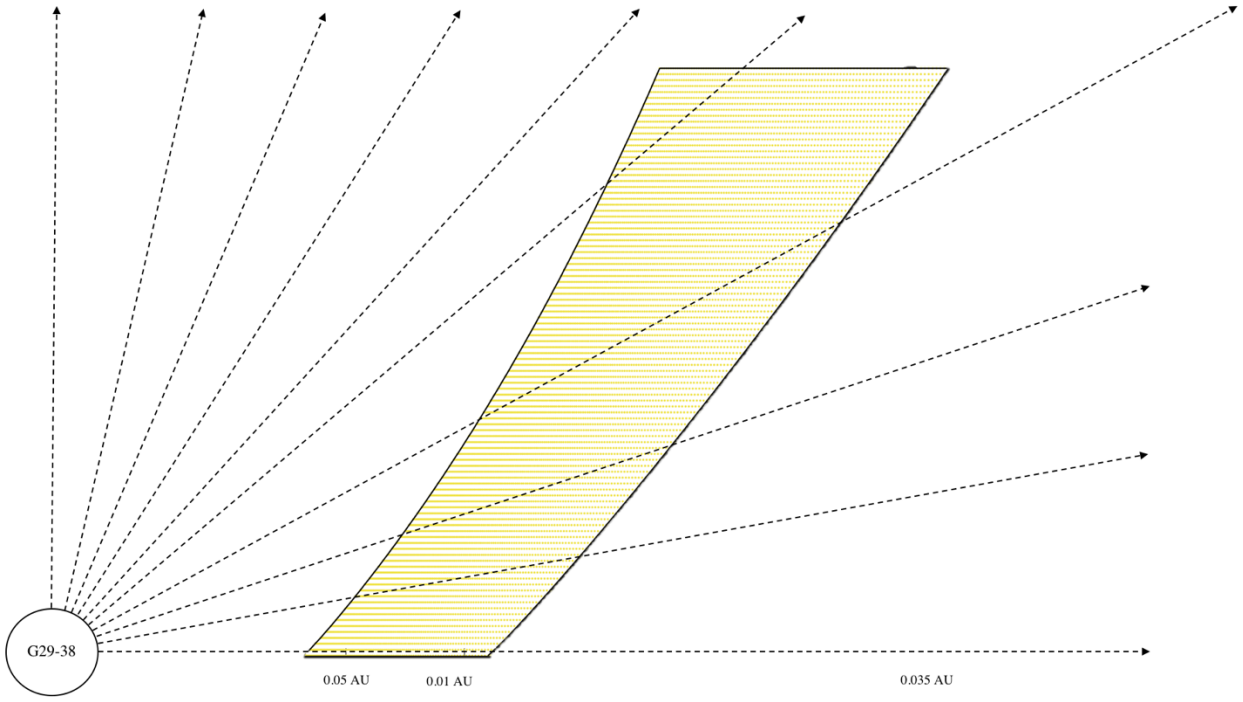

Figure 17. This figure shows the shape of a disk-wind for G29-38 placed by the star. The dotted lines coming from G29-38 represent the direct path of the starlight when it leaves the white dwarf. At some angles, the starlight can travel past the outflow without interacting. This starlight is better observed at lower inclination angles.

At 60-degree inclination, starlight will be forced to travel through the bottom regions of the wind which are the densest (*see Figure 15*) and thus the IR flux relative to the direct visible

flux will be maximized. It is also important to note that while all the plots in *Figure 16* have been normalized to the blackbody curve for easier model to model comparison, in reality for the case of the 60-degree inclination angle, the optical flux decreases which is why the ratio of infrared to optical flux increases.

In the asteroid-mass wind, though the angles of inclination travel through various heights of the outflow, the optical depths are so low throughout the wind that it is essentially transparent (*see Table A.2*) which is unlike the Jupiter and Earth mass cases. This explains why the flux levels remain relatively equal with each angle of inclination.

In the case of the x-wind models, we see similar changes to the flux with inclination angle throughout each model as we see in the disk-wind models (*See Figure 16*). The asteroid-mass model again doesn't change much in flux with the different inclination angles. This is due to the same reason as the disk-wind model – the one asteroid wind is essentially transparent. A visualization for the x-wind model shows the shape of the model with various lines of sight from the star (*See Figure 18*). In the x-wind plots, the difference between 40 degrees and 30 degrees is much sharper than the disk winds. This is because in our code we artificially cut off the height of the x-wind at $5R_M$. In *Figure 18*, let's correspond the fourth line from the left with a 30-degree inclination and the fifth line from the left with a 40-degree inclination. The 40-degree inclination passes through more wind than the 30-degree inclination. In the disk wind case, the difference between the 30-degree and 40-degree inclinations doesn't really matter because the density drops rapidly with height. However, in the x-wind case, the difference between the 30-degree and 40-degree inclinations is significant because the top of the wind is still very dense. This is why the flux for the x-winds is on average much higher than the flux of the disk-winds no matter what inclination angle at which we are viewing the star.

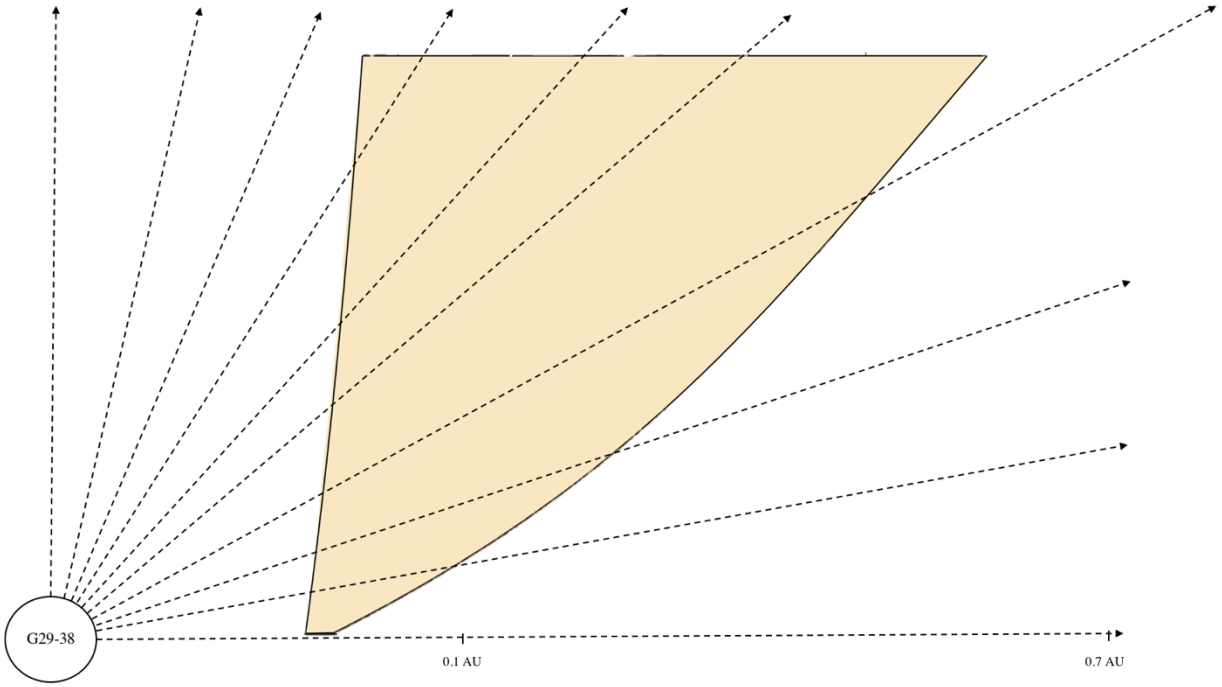

Figure 18. This figure shows the shape of an x-wind for G29-38. The dotted lines coming from G29-38 represent the direct path of the starlight when it leaves the white dwarf. At some angles, the starlight can travel past the outflow without interacting.

If dusty outflows exist in other dusty white dwarf systems, and within those systems the geometry and magnetic field of the star-disk system is comparable to G29-38, then the extreme and subtle differences between the spectral energy distribution of various dusty white dwarfs could merely be a consequence of randomly distributed inclination angles. An outflow with a wider angle such as disk wind model G or E, or with a flat or torus shaped disk like those previously modeled in the literature, it would be harder to get strong inclination effects. For a very flat thin disk, the inclination angle would need to be at 90 degrees to block the star. Therefore, it is highly unlikely that other potential cases of low stellar flux to high IR flux would be explained by such a scenario. This is another reason why vertical winds could be a more logical model than a disk or flared torus because the outflows that we modeled allow for variation in spectral energy distribution for a much larger range of inclinations compared to the non-outflow model.

Outflows and Rotation

When outflows are launched from the disk, they can take the angular momentum from the star. This means that outflows could ultimately result in a slower rotating star. T-tauri stars are slow rotators because of their outflows. If outflows are relevant to the G29-38's strong IR excess, then other dusty white dwarfs with similar IR excess would rotate more slowly than white dwarfs of the same age but without IR emissions. If the rotation of other dusty white dwarfs is comparable to the rotation of G29-38 then it is possible that outflows are significant in other white dwarf systems too.

Over time, the outflows launched from the disk will deplete the disk mass to a point where outflows would no longer be able to exist. This places a different timescale on dusty white dwarf systems than the timescales from estimates of accretion rates or Poynting-Robertson drag that describe how long it would take to lose the dust in the disk to the pull of the star. Therefore, a more careful examination of outflows may predict different observed lifetimes of dusty white dwarfs.

The vertical extend of outflows provides another unique effect. Outflows can shield any material behind them. This was examined in the protostellar case as a possible explanation for the variability at longer wavelengths. Small changes in the outflow rate (and thus the mass contained within some amount of wind) can easily change the flux levels in the NIR and thus are also a possible way to explain variability. As more studies reveal the variability of the spectral energy distribution for G29-38 over time, it will become easier to constrain the mass loss rates of the outflow winds.

Chapter VI. Conclusion and Directions for Further Work

The toy models created for the outflows of G29-38 are novel representations of the system. We find that over all, the disk-wind and x-wind models can separately recreate the 10-micron silicate feature and the NIR excess in the spectral energy distribution of G29-38. This proof of concept will further motivate future work in understanding outflows in isolated magnetic white dwarfs with dusty circumstellar environments as well as allow us to expand our disk-wind models and x-wind models.

Previous disk models used to recreate the SED plots for G29-38 estimated that the amount of dust mass needed would be ~10^{19} grams (Reach et al., 2009). In future work, we would like to expand our objects from Hygeia mass asteroids to a Ceres mass asteroid because the mass jump between our 5-asteroid model to our 1 Earth model is quite extreme. Ceres mass is about 10^{24} grams. In our models, a Ceres-mass disk would create a 10^{21} g mass wind. In our models, we also used a gas to dust ratio of 100. Therefore, the amount of dust in the 10^{21} g mass wind would be about 10^{19} grams, which is comparable to the literature. If the best fit for the SED results from an object with a Ceres-like mass, perhaps this could indicate that the object that was tidally destroyed by G29-38 was a Kuiper-belt like contribution that got perturbed into the white dwarf system. Further searches for "cold" populations of dust could help confirm this hypothesis.

Observationally, outflows usually involve MIR variability. In our code, a large number of photon packets is required to bin wavelengths in the MIR range (*See Figure 16*). Due to time constraints, many of our simulations were not sampled with large enough photon packet numbers to accurately see the shape of the MIR wavelength. We would like to explore our models with higher photon packet sampling to a) produce a crisper picture of the NIR and 10-micron feature and b) investigate the MIR range of photons wavelengths. Additionally, we would need to extend

our physical models spatially in height and potentially in radius to explore longer wavelength emission.

To expand our analysis of the inclination angle effects, in the future we would like to integrate the optical depths of the photon as it travels through the system to study the relationship of flux and optical depth through various points of the wind.

In conclusion, the outflow models we present in this project indicate that it is possible to model the observed spectral energy distribution features of G29-38 with magnetically supported and vertically distributed outflows.

Appendix A.

Table A.1 *The following table presents the modeled parameters for all 72 simulations. B is the magnetic field limit, R_M is the magnetic truncation radius, and R_{OUT} is the outer boundary of the disk. The outer boundaries of the disk that were scaled to $10R_L$ are highlighted in grey and the outer boundaries that were scaled to $11R_L$ are highlighted in blue*

#	Object	Disk Mass	Wind Mass	Wind	B	R_M	R_{OUT}
1	1 Asteroid	8.276×10^{22}	8.276×10^{20}	Disk	2.5 kG	4.7053×10^{10} cm	3.8334×10^{11}
2	1 Asteroid	8.276×10^{22}	8.276×10^{20}	Disk	20 kG	1.5440×10^{11} cm	3.8334×10^{11}
3	1 Asteroid	8.276×10^{22}	8.276×10^{20}	Disk	2.5 kG	9.4106×10^{10} cm	3.8334×10^{11}
4	1 Asteroid	8.276×10^{22}	8.276×10^{20}	Disk	20 kG	3.0879×10^{11} cm	3.8334×10^{11}
5	3 Asteroids	2.483×10^{23}	2.483×10^{21}	Disk	2.5 kG	4.7053×10^{10} cm	3.8334×10^{11}
6	3 Asteroids	2.483×10^{23}	2.483×10^{21}	Disk	20 kG	1.5440×10^{11} cm	3.8334×10^{11}
7	3 Asteroids	2.483×10^{23}	2.483×10^{21}	Disk	2.5 kG	9.4106×10^{10} cm	3.8334×10^{11}
8	3 Asteroids	2.483×10^{23}	2.483×10^{21}	Disk	20 kG	3.0879×10^{11} cm	3.8334×10^{11}
9	5 Asteroids	4.138×10^{23}	4.138×10^{21}	Disk	2.5 kG	4.7053×10^{10} cm	3.8334×10^{11}
10	5 Asteroids	4.138×10^{23}	4.138×10^{21}	Disk	20 kG	1.5440×10^{11} cm	3.8334×10^{11}
11	5 Asteroids	4.138×10^{23}	4.138×10^{21}	Disk	2.5 kG	9.4106×10^{10} cm	3.8334×10^{11}
12	5 Asteroids	4.138×10^{23}	4.138×10^{21}	Disk	20 kG	3.0879×10^{11} cm	3.8334×10^{11}
13	1 Earths	5.972×10^{27}	5.972×10^{25}	Disk	2.5 kG	4.7053×10^{10} cm	2.6389×10^{11}
14	1 Earths	5.972×10^{27}	5.972×10^{25}	Disk	20 kG	1.5440×10^{11} cm	2.6389×10^{11}
15	1 Earths	5.972×10^{27}	5.972×10^{25}	Disk	2.5 kG	9.4106×10^{10} cm	2.6389×10^{11}
16	1 Earths	5.972×10^{27}	5.972×10^{25}	Disk	20 kG	3.0879×10^{11} cm	5.2779×10^{11}
17	3 Earths	1.792×10^{28}	1.792×10^{26}	Disk	2.5 kG	4.7053×10^{10} cm	1.8298×10^{11}
18	3 Earths	1.792×10^{28}	1.792×10^{26}	Disk	20 kG	1.5440×10^{11} cm	1.8298×10^{11}

19	3 Earths	1.792×10^{28}	1.792×10^{26}	Disk	2.5 kG	9.4106×10^{10} cm	1.8298×10^{11}
20	3 Earths	1.792×10^{28}	1.792×10^{26}	Disk	20 kG	3.0879×10^{11} cm	3.6595×10^{11}
21	5 Earths	2.986×10^{28}	2.986×10^{26}	Disk	2.5 kG	4.7053×10^{10} cm	1.5433×10^{11}
22	5 Earths	2.986×10^{28}	2.986×10^{26}	Disk	20 kG	1.5440×10^{11} cm	3.0866×10^{11}
23	5 Earths	2.986×10^{28}	2.986×10^{26}	Disk	2.5 kG	9.4106×10^{10} cm	1.5433×10^{11}
24	5 Earths	2.986×10^{28}	2.986×10^{26}	Disk	20 kG	3.0879×10^{11} cm	4.6299×10^{11}
25	1 Jupiter	1.898×10^{30}	1.898×10^{28}	Disk	2.5 kG	4.7053×10^{10} cm	4.3324×10^{11}
26	1 Jupiter	1.898×10^{30}	1.898×10^{28}	Disk	20 kG	1.5440×10^{11} cm	4.3324×10^{11}
27	1 Jupiter	1.898×10^{30}	1.898×10^{28}	Disk	2.5 kG	9.4106×10^{10} cm	4.3324×10^{11}
28	1 Jupiter	1.898×10^{30}	1.898×10^{28}	Disk	20 kG	3.0879×10^{11} cm	4.3324×10^{11}
29	3 Jupiters	5.694×10^{30}	5.694×10^{28}	Disk	2.5 kG	4.7053×10^{10} cm	3.0039×10^{11}
30	3 Jupiters	5.694×10^{30}	5.694×10^{28}	Disk	20 kG	1.5440×10^{11} cm	3.0039×10^{11}
31	3 Jupiters	5.694×10^{30}	5.694×10^{28}	Disk	2.5 kG	9.4106×10^{10} cm	3.0039×10^{11}
32	3 Jupiters	5.694×10^{30}	5.694×10^{28}	Disk	20 kG	3.0879×10^{11} cm	6.0080×10^{11}
33	5 Jupiters	9.400×10^{30}	9.400×10^{28}	Disk	2.5 kG	4.7053×10^{10} cm	2.5336×10^{11}
34	5 Jupiters	9.400×10^{30}	9.400×10^{28}	Disk	20 kG	1.5440×10^{11} cm	2.5336×10^{11}
35	5 Jupiters	9.400×10^{30}	9.400×10^{28}	Disk	2.5 kG	9.4106×10^{10} cm	2.5336×10^{11}
36	5 Jupiters	9.400×10^{30}	9.400×10^{28}	Disk	20 kG	3.0879×10^{11} cm	5.0673×10^{11}
37	1 Asteroid	8.276×10^{22}	8.276×10^{20}	X	2.5 kG	4.7053×10^{10} cm	3.8334×10^{11}
38	1 Asteroid	8.276×10^{22}	8.276×10^{20}	X	20 kG	1.5440×10^{11} cm	3.8334×10^{11}
39	1 Asteroid	8.276×10^{22}	8.276×10^{20}	X	2.5 kG	9.4106×10^{10} cm	3.8334×10^{11}
40	1 Asteroid	8.276×10^{22}	8.276×10^{20}	X	20 kG	3.0879×10^{11} cm	3.8334×10^{11}

41	3 Asteroids	2.483×10^{23}	2.483×10^{21}	X	2.5 kG	4.7053×10^{10} cm	3.8334×10^{11}
42	3 Asteroids	2.483×10^{23}	2.483×10^{21}	X	20 kG	1.5440×10^{11} cm	3.8334×10^{11}
43	3 Asteroids	2.483×10^{23}	2.483×10^{21}	X	2.5 kG	9.4106×10^{10} cm	3.8334×10^{11}
44	3 Asteroids	2.483×10^{23}	2.483×10^{21}	X	20 kG	3.0879×10^{11} cm	3.8334×10^{11}
45	5 Asteroids	4.138×10^{23}	4.138×10^{21}	X	2.5 kG	4.7053×10^{10} cm	3.8334×10^{11}
46	5 Asteroids	4.138×10^{23}	4.138×10^{21}	X	20 kG	1.5440×10^{11} cm	3.8334×10^{11}
47	5 Asteroids	4.138×10^{23}	4.138×10^{21}	X	2.5 kG	9.4106×10^{10} cm	3.8334×10^{11}
48	5 Asteroids	4.138×10^{23}	4.138×10^{21}	X	20 kG	3.0879×10^{11} cm	3.8334×10^{11}
49	1 Earths	5.972×10^{27}	5.972×10^{25}	X	2.5 kG	4.7053×10^{10} cm	2.6389×10^{11}
50	1 Earths	5.972×10^{27}	5.972×10^{25}	X	20 kG	1.5440×10^{11} cm	2.6389×10^{11}
51	1 Earths	5.972×10^{27}	5.972×10^{25}	X	2.5 kG	9.4106×10^{10} cm	2.6389×10^{11}
52	1 Earths	5.972×10^{27}	5.972×10^{25}	X	20 kG	3.0879×10^{11} cm	5.2779×10^{11}
53	3 Earths	1.792×10^{28}	1.792×10^{26}	X	2.5 kG	4.7053×10^{10} cm	1.8298×10^{11}
54	3 Earths	1.792×10^{28}	1.792×10^{26}	X	20 kG	1.5440×10^{11} cm	1.8298×10^{11}
55	3 Earths	1.792×10^{28}	1.792×10^{26}	X	2.5 kG	9.4106×10^{10} cm	1.8298×10^{11}
56	3 Earths	1.792×10^{28}	1.792×10^{26}	X	20 kG	3.0879×10^{11} cm	3.6595×10^{11}
57	5 Earths	2.986×10^{28}	2.986×10^{26}	X	2.5 kG	4.7053×10^{10} cm	1.5433×10^{11}
58	5 Earths	2.986×10^{28}	2.986×10^{26}	X	20 kG	1.5440×10^{11} cm	3.0866×10^{11}
59	5 Earths	2.986×10^{28}	2.986×10^{26}	X	2.5 kG	9.4106×10^{10} cm	1.5433×10^{11}
60	5 Earths	2.986×10^{28}	2.986×10^{26}	X	20 kG	3.0879×10^{11} cm	4.6299×10^{11}
61	1 Jupiter	1.898×10^{30}	1.898×10^{28}	X	2.5 kG	4.7053×10^{10} cm	4.3324×10^{11}
62	1 Jupiter	1.898×10^{30}	1.898×10^{28}	X	20 kG	1.5440×10^{11} cm	4.3324×10^{11}

63	1 Jupiter	1.898×10^{30}	1.898×10^{28}	X	2.5 kG	9.4106×10^{10} cm	4.3324×10^{11}
64	1 Jupiter	1.898×10^{30}	1.898×10^{28}	X	20 kG	3.0879×10^{11} cm	4.3324×10^{11}
65	3 Jupiters	5.694×10^{30}	5.694×10^{28}	X	2.5 kG	4.7053×10^{10} cm	3.0039×10^{11}
66	3 Jupiters	5.694×10^{30}	5.694×10^{28}	X	20 kG	1.5440×10^{11} cm	3.0039×10^{11}
67	3 Jupiters	5.694×10^{30}	5.694×10^{28}	X	2.5 kG	9.4106×10^{10} cm	3.0039×10^{11}
68	3 Jupiters	5.694×10^{30}	5.694×10^{28}	X	20 kG	3.0879×10^{11} cm	6.0080×10^{11}
69	5 Jupiters	9.400×10^{30}	9.400×10^{28}	X	2.5 kG	4.7053×10^{10} cm	2.5336×10^{11}
70	5 Jupiters	9.400×10^{30}	9.400×10^{28}	X	20 kG	1.5440×10^{11} cm	2.5336×10^{11}
71	5 Jupiters	9.400×10^{30}	9.400×10^{28}	X	2.5 kG	9.4106×10^{10} cm	2.5336×10^{11}
72	5 Jupiters	9.400×10^{30}	9.400×10^{28}	X	20 kG	3.0879×10^{11} cm	5.0673×10^{11}

Table A.2 *The following table presents the average optical depths through the base of the disk wind for every model. The optical depth is an average over the 500 nm photon optical depth and the FUV photon optical depth.*

Object	Magnetic Field	ξ	Optical Depth
1 Asteroid	2.5 kG	$\xi = 0.5$	0.5363405
	2.5 kG	$\xi = 1$	0.1025635
	20 kG	$\xi = 0.5$	0.0618635
	20 kG	$\xi = 1$	0.02881885
3 Asteroids	2.5 kG	$\xi = 0.5$	0.6339825
	2.5 kG	$\xi = 1$	0.309465
	20 kG	$\xi = 0.5$	0.18565
	20 kG	$\xi = 1$	0.0864702
5 Asteroids	2.5 kG	$\xi = 0.5$	1.068585
	2.5 kG	$\xi = 1$	0.516011
	20 kG	$\xi = 0.5$	0.3090205
	20 kG	$\xi = 1$	0.144097
1 Earth	2.5 kG	$\xi = 0.5$	55358.4
	2.5 kG	$\xi = 1$	27227.35
	20 kG	$\xi = 0.5$	16016.1
	20 kG	$\xi = 1$	4004.42
3 Earths	2.5 kG	$\xi = 0.5$	239486
	2.5 kG	$\xi = 1$	115060.5
	20 kG	$\xi = 0.5$	16634.5
	20 kG	$\xi = 1$	66352.25
5 Earths	2.5 kG	$\xi = 0.5$	223665
	2.5 kG	$\xi = 1$	223726
	20 kG	$\xi = 0.5$	69376.1
	20 kG	$\xi = 1$	22505.95
1 Jupiter	2.5 kG	$\xi = 0.5$	11088400
	2.5 kG	$\xi = 1$	5343040
	20 kG	$\xi = 0.5$	3209795
	20 kG	$\xi = 1$	1508905
3 Jupiters	2.5 kG	$\xi = 0.5$	1.3581525×10^7
	2.5 kG	$\xi = 1$	2.29088×10^7
	20 kG	$\xi = 0.5$	1.3571×10^7
	20 kG	$\xi = 1$	3.396705×10^6
5 Jupiters	2.5 kG	$\xi = 0.5$	9.090035×10^7
	2.5 kG	$\xi = 1$	4.459815×10^7
	20 kG	$\xi = 0.5$	2.589265×10^7
	20 kG	$\xi = 1$	6.523645×10^6

Table A.3 *The following table presents the average optical depths through the base of the x-wind for every model. The optical depth is an average over the 500 nm photon optical depth and the FUV photon optical depth.*

Object	Magnetic Field	ξ	Optical Depth
1 Asteroid	2.5 kG	$\xi = 0.5$	0.00135
	2.5 kG	$\xi = 1$	0.00332
	20 kG	$\xi = 0.5$	0.00012
	20 kG	$\xi = 1$	0.00003
3 Asteroids	2.5 kG	$\xi = 0.5$	0.00388
	2.5 kG	$\xi = 1$	0.00367
	20 kG	$\xi = 0.5$	0.00032
	20 kG	$\xi = 1$	0.00009
5 Asteroids	2.5 kG	$\xi = 0.5$	0.00021
	2.5 kG	$\xi = 1$	0.00061
	20 kG	$\xi = 0.5$	0.00045
	20 kG	$\xi = 1$	0.00006
1 Earth	2.5 kG	$\xi = 0.5$	59.3842
	2.5 kG	$\xi = 1$	23.2356
	20 kG	$\xi = 0.5$	12.0145
	20 kG	$\xi = 1$	3.00342
3 Earths	2.5 kG	$\xi = 0.5$	249.445
	2.5 kG	$\xi = 1$	103.091
	20 kG	$\xi = 0.5$	12.6345
	20 kG	$\xi = 1$	66.3762
5 Earths	2.5 kG	$\xi = 0.5$	22.3665
	2.5 kG	$\xi = 1$	27.3726
	20 kG	$\xi = 0.5$	72.3761
	20 kG	$\xi = 1$	23.50595
1 Jupiter	2.5 kG	$\xi = 0.5$	11278.30
	2.5 kG	$\xi = 1$	5548.050
	20 kG	$\xi = 0.5$	3139.795
	20 kG	$\xi = 1$	1309.505
3 Jupiters	2.5 kG	$\xi = 0.5$	1.45655×10^4
	2.5 kG	$\xi = 1$	2.58988×10^4
	20 kG	$\xi = 0.5$	1.2673×10^4
	20 kG	$\xi = 1$	3.8945×10^3
5 Jupiters	2.5 kG	$\xi = 0.5$	9.5971×10^4
	2.5 kG	$\xi = 1$	4.7892×10^4
	20 kG	$\xi = 0.5$	2.7881×10^4
	20 kG	$\xi = 1$	6.4235×10^4

Table A.4 *The same three simulated disk wind models, with their x-wind model counterparts, are shown in the table with their magnetic truncation radii, the width of the wind launched from the disk, the height of the wind, and the angle the wind makes with the accretion disk. For the x-winds, the width of the wind is 0.1132* R_M*, and for all wind models, the height of the wind scales as 5* R_M*.*

Model	Wind Type	R_M *(cm)*	Wind Width *(cm)*	Wind Height *(cm)*	θ *(degrees)*
1 Asteroid	Disk Wind	3.088×10^{11}	7.455×10^{10}	1.544×10^{12}	87.24
5 Earths	Disk Wind	9.411×10^{10}	6.0224×10^{10}	4.7055×10^{11}	82.71
1 Jupiter	Disk Wind	1.544×10^{11}	2.7884×10^{11}	7.77×10^{11}	70.23
1 Asteroid	X-wind	3.088×10^{11}	3.4376×10^{11}	1.544×10^{12}	77.45
5 Earths	X-wind	9.411×10^{10}	1.0476×10^{11}	4.7055×10^{11}	77.45
1 Jupiter	X-wind	1.544×10^{11}	1.7299×10^{11}	7.77×10^{11}	77.45

References.

Alcock et al., "On the number of comets around other single stars", *The Astrophysical Journal*, 302:462-467, 1 March 1986

Bans et al., "A Disk-Wind Model for the Near-Infrared Excess Emission in Protostars", *The Astrophysical Journal*, 758:100-117, 2012

Barucci et al., "10 Hygiea: ISO Infrared Observations", *Icarus*, 156(1):202-210, March 2002

Blandford & Payne, "Hydromagnetic flows from accretion disks and the production of radio jets", *Monthly Notices of the Royal Astronomical Society,* 199:883-903, 1982 June

Chary et al., "Observational Constraints on the Origin of Metals in Cool DA-Type White Dwarfs", *The Universe as seen by ISO*. eds. P. Cox & M. F. Kessler. ESA-SP 427., p. 289, March 1999

Debes et al., "Cool Customers in the Stellar Graveyard I: Limits to Extrasolar Planets Around the White Dwarf G29-38", *The Astrophysical Journal*, 633:1168-1164, 2005

Duerbeck, H.W., "ZZ Ceti variables", *Light Curves of Variable Stars: A Pictorial Atlas*, eds. C. Sterken and C. Jaschek, Cambridge University Press, 108, 29 September 2005

Dupuis et al., "A study of metal abundance patterns in cool white dwarfs. I – time dependent calculations of gravitational setting", *The Astrophysical Journal Supplement Series*, 82(2):505-521, September 1992

Dupuis et al., "A study of metal abundance patterns in cool white dwarfs. II – Simulations of accretion episodes", *The Astrophysical Journal Supplemt Series*, 84(1):73-89, December 1992

Dupuis et al., "A study of metal abundance patterns in cool white dwarfs. III – Comparison of the predicttions of the two-phase accretion model with observations", *The Astrophysical Journal Supplement Series*, 87(1):345-365, 1993

Edwards et al., "Probing T Tauri Accretion and Outflow with 1 Micron Spectroscopy", *The Astrophysical Journal*, 646:318-341, 20 July 2006

Farihi, J. "Circumstellar Debris and Pollution at White Dwarf Stars", *New Astronomy Reviews*, 11 April 2016

Farihi et al., "Magnetism, X-rays and accretion rates in WD 1145+017 and other polluted white dwarf systems", *Monthly Notices of the Royal Astronomical Society*, Volume 474, Issue 1, 11 February 2018, Pages 947–960 24 October 2017

Farihi et al., "Rocky planetesimals as the origin of metals in DZ stars", *Monthly Notices of the Royal Astronomical Society*, 17 July 2017

Froning, Cynthia S., "Observations of Outflows in Cataclysmic Variables" *The Astrophysics of Cataclysmic Variables and Related Objects*, ASP Conf. Ser., eds. J.M. Hameury and J.P. Lasota, 7 October 2004

Fusillo et al., "Can magnetic fields suppress convection in the atmosphere of cool white dwarfs? A case study on WD2105-820", *Solar and Stellar Astrophysics*, 2017

Hermes et al., "A new timescale for period change in the pulsating DA white dwarf WD 0111+0018", *The Astrophyscial Journal*, 766(1) 2013

Jordan et al., "The fraction of DA white dwarfs with kilo-Gauss magnetic fields", *Astronomy and Astrophysics*, 462(3):1097-1101, 11 February 2007

Jura, M. "A Tidally Disrupted Asteroid Around the White Dwarf G29-38", *The Astrophysical Jounral,* 584:L91-L94, 20 February 2003

Jura et al., "Externally-Polluted White Dwarfs with Dust Disks", *The Astrophysical Journal*, 663:1285-1290, 2007

Jura et al., "Six White Dwarfs with Circumstellar Silicates", *The Astronomical Journal*, 137(2), 28 January 2009

Jura et al., "X-ray and Infrared Observations of Two Externally-Polluted White Dwarfs", *The Astrophyscial Journal*, 699:1473-1479, 2009

Kawaler, Steven D. "White Dwarf Rotation: Observations and Theory", *Stellar Rotation* Proceedings IAU Symposium No. 215, Andre Maeder & Philippe Eenens, eds., November 2002

Koester et al., "Metals in the variable DA G29-38", *Astronomy and Astrophysics*, 320:L57-L59, 1997

Koester, D., "Accretion and diffusion in white dwarfs. New diffusion timescales and applications to GD362 and G29-38", *Astronomy and Astrophysics*, 2009

Königl, A. & E. Pudritz, "Disk Winds and the Accretion—Outflow Connection", Protostars and Planets IV, ed. V. Mannings, A. Boss, and S. Russell (Arizona: University of Arizona Press), 1999

Kuchner et al., "Keck Speckle Imaging of the White Dwarf G29-38: No Brown Dwarf Companion Detected", *The Astrophysical Journal Letters*, 508(1), 1998

Kurz D.W. & Martinez, P. "Long-term monitoring of cyclic frequency variability in rapidly oscilating Ap stars at the Sutherland Station of the South African Astronomical Oberservatory", *The Impact of Long Term Monitoring on Variable Star Research: Astrophysics, Instrumentation, Data Handling, Archiving*, eds. C. Sterken, Mart de Groot, Springer Science & Business Media, 6 December 2012

Long et al., "Locking of the Rotation of Disk-Accreting Magnetized Stars", *The Astrophysical Journal*, 634:1214-1222, 2005 December 1

Montgomery, M. H., "Mapping Convection Using Pulsating White Dwarf Stars", *New Horizons in Astronomy: Frank N. Bash Symposium ASP Conference Series*, Vol. 352, Proceedings of the Conference Held 16-18 October, 2005 at The University of Texas, Austin, Texas, USA, p.261

Pudritz et al., "Disk Winds, Jets, and Outflows: Theoretical and Computational Foundations" *Protostars and Planets V*, B. Reipurth, D. Jewitt, and K. Keil (eds.), University of Arizona Press, Tucson, 2006

Reach et al., "The Dust Cloud Around the White Dwarf G29-38", *The Astrophysical Journal*, 635:L161–L164, 2005 December 20

Reach et al., "The Dust Cloud around the White Dwarf G 29-38. 2. Spectrum from 5-40 μm and mid-infrared photometric variability", *The Astrophysical Journal*, 693: 697-712, 2009

Robinson et. al, *The Astrophysical Journal*, 259:219

Safier, P., "Centrifugally driven winds from Protostellar disks. I-Wind model and thermal structure", *The Astrophysical Journal*, 408(1):115-159, 1993

Spruit & Taam, "An Instability Associated with a Magnetosphere-Disk Interaction", *The Astrophysical Journal*, 402:593-604, 10 January 1993

Ryden, B., "Chapter 10: Advanced Accretion Disks", Lecture Notes, Ohio State University, 2007

S. Xu et al., "Elemental Compositions of Two Extrasolar Rocky Planetesimals", *The Astrophysical Journal*, volume 783 number 2 2014 February 19

Shu et al., "Magnetocentrifugally driven flows from young stars and disks I. A Generalized Model" *The Astrophysical Journal* 429: 781-796, 10 July 1994

Shu F.H., Shang H. "Protostellar X-rays, Jets, and Bipolar Outflows", *Herbig-Haro Flows and the Birth of Low Mass Stars*, eds. Reipurth B., Bertout C., v.182, 1997

Sokoloski & Kenyon, "CH Cygni. I. Observational Evidence for Disk-Jet Connection" *The Astrophysical Journal*, 584: 1021-1026, 20 Feb 2003

Thompson et al., "Pulsational Mapping of Calcium Across the Surface of a White Dwarf", *The Astrophysical Journal*, 714:296-308, 2010 May 1

Von Hippel et al., "The New Class of Dusty DAZ White Dwarfs", *The Astrophysical Journal*, 662:544–551, 10 June 2007

Y. -M. Wang, "Location of the Inner Radius of a Magnetically Threaded Accretion Disk", *The Astrophysical Journal*, 465:L111-L113, 1996 July 10

Zuckerman, B. & E.E. Becklin, "Excess infrared radiation from a white dwarf—an orbiting brown dwarf?", *Nature*, 330:138-140, 18 November 1987